The Hong Kong Polytechnic University

Department of Applied Physics

STRUCTURAL AND DIELECTRIC PROPERTIES OF EPITAXIAL PEROVSKITE TITANATE THIN FILMS

WU Zhenping

A thesis submitted in partial fulfillment of the requirements

for the degree of Master of Philosophy

October 2008

CERTIFICATE OF ORIGINALITY

I hereby declare that this thesis is my own work and that, to the best of my knowledge and belief, it reproduces no material previously published or written, nor material that has been accepted for the award of any other degree or diploma, except where due acknowledgement has been made in the text.

_____(Signed)

_____WU Zhenping_____(Name of student)

ABSTRACT

In recent years, tunable and affordable high-frequency microwave devices have been widely studied for the next generation of communication and radar system. Perovskite titanates such as $SrTiO_3$ have relatively large and field-dependent dielectric constant and low loss, which are considered to be one of the most promising candidates for such application. Structural and dielectric properties of perovskite titanates are important in comprising those materials into devices.

In the present thesis, the multilayer of $SrTiO_3/YBa_2Cu_3O_y$ was deposited using laser molecular beam epitaxy technique. The growth mode of the films was investigated using *in-situ* reflection high energy electron diffraction. The crystal structure in $SrTiO_3/YBa_2Cu_3O_y$ multilayer was measured by X-ray diffraction measurement. The morphology was determined with atomic force microscope. The Raman scattering measurement is employed to study the lattice dynamic properties of the heterostructure in the temperature range from 10 to 300 K. The effects of temperature and frequency on the dielectric properties of $SrTiO_3$ thin films were evaluated.

Secondly, epitaxial $SrTiO_3$ films were grown on GaAs (001) substrates without any buffer layers using laser molecular beam epitaxy technique. The reflection high energy electron diffraction observations have revealed that a layer-by-layer growth of

$SrTiO_3$ was achieved by optimizing deposition process. The crystalline orientation of the as-grown $SrTiO_3$ (001) films rotates 45° in plane with respect to the GaAs (001) substrates. Atomic force microscope studies show that these films possess atomically flat surfaces. The $SrTiO_3$/GaAs interface with a sharp interface was investigated by transmission electron microscopy. The dielectric properties of the heterostructure were also investigated. Our results have clearly demonstrated the practicality of integrating perovskite oxide thin films with GaAs substrates.

Thirdly, Ferroelectric $BaTiO_3$ thin films were epitaxially grown on (001) GaAs substrate using $SrTiO_3$ as a buffer layer by laser molecular beam epitaxy. The interface structure was analyzed by means of reflection high energy electron diffraction and transmission electron microscopy. The perovskite $SrTiO_3$ buffer layer presents a body centered cubic structure by forming 10nm-thick interfacial layer, with the [100]$SrTiO_3$//[110]GaAs in-plane relationship. Thereupon, a highly c-oriented $BaTiO_3$ was grown on $SrTiO_3$/GaAs in a layer by layer mode with a sharp interface and a significant reduction of mismatch-related defects. The $BaTiO_3$ (150nm)/$SrTiO_3$(10nm)/GaAs heterostructure demonstrates ferroelectric hysteresis behavior with a remnant polarization of 2.5μC/cm^2 and a small leakage current density of 2.9×10^{-7} A/cm^2 at 200 kV. The observation shows that it is feasible for integrated device applications by introducing $SrTiO_3$ buffer layer at the interface between $BaTiO_3$ film and GaAs.

LIST OF PUBLICATIONS

1. Z. P. Wu, W. Huang, K. H. Wong, and J. H. Hao, "Structural and dielectric properties of epitaxial $SrTiO_3$ films grown directly on GaAs substrates by laser molecular beam epitaxy", *Journal of Applied Physics*, 104, 054103 (2008)

2. Z. P. Wu, J. L. Li, and J. H. Hao, "Effect of preparation on the growth mode and structure in Laser MBE grown multilayer of $SrTiO_3$ and $YBa_2Cu_3O_y$", *Proc. of SPIE Vol.* 6643, 66430L (2007)

3. Z. P. Wu, W. Huang, J. H. Hao, and Q. M. Zhang, "Structural, dielectric and optical Raman characterization of laser MBE grown $SrTiO_3$ based heterostructure", submitted to *Solid State Sciences.*

4. W. Huang, Z. P. Wu, and J. H. Hao, "Electrical properties of ferroelectric $BaTiO_3$ thin film on $SrTiO_3$ buffered GaAs by laser molecular beam epitaxy", *Applied Physics Letters*, 94, 032905 (2009)

ACKNOWLEDGEMENTS

I would like to extend thanks to a number of people who have contributed to the completion of this project. First of all, I sincerely would like to express my sincere gratitude to my supervisors, Dr. J. H. Hao and Prof. K. H. Wong, for their guidance, encouragement and the opportunity to do research in a fascinating field. I would also like to thank Prof. H. L. W. Chan, Prof. C. L. Choy, Dr. J. Y. Dai, Dr. F. Yan and Dr. Y. Wang for their assistance on my research and coursework studies.

I would also like to thank Dr W. Huang, Dr. J. L. Li and Dr. S. X. Wang for providing invaluable supports and suggestions to this work.

I wish to acknowledge Mr. M. N. Yeung of the Materials Research Centre for his assistance in the structure characterization.

I would like to give my thanks to my colleagues and friends in AP: Dr. P. F. Lee, Dr. D. Y. Wang, Dr. Z. L. Wang, Dr. G. Y. Wang, Dr. X. Y. Zhou, Miss. K. C. Chan, Miss. H. L. Li, Miss. P. Yun, Mr. H. Li, Mr. J. X. Zhang, Mr. M. X. Cao, Mr. Y. B. Chan and Mr. J. Liu, I owe special thanks to their assistance and discussions in the research work.

I gratefully acknowledge the financial support from the Department of Applied Physics and the Centre for Smart Materials of the Hong Kong Polytechnic University.

Finally, I would like to express my deepest appreciations to my parents for their support, encouragement and enduring love over the years. Without you this would not have been possible.

TABLE OF CONTENTS

LIST OF FIGURE CAPTIONS

LIST OF TABLE CAPTIONS

LIST OF SYMBOLS

Symbol	Description
r	radius
ε	relative permittivity
C	Curie constant
T_0	Curie-Weiss temperature
T_c	Curie temperature
E	electric field
H	magnetic field
P_r	remnant polarization
λ	wavelength
ε'	the real part of the permittivity
ε''	the imaginary component of the permittivity
$\tan\delta$	the loss tangent
K	figure of merit
$\varepsilon(T, E)$	the dielectric constant under the electrical field
$\varepsilon(T, 0)$	the dielectric constant under zero field
$E_0(T)$	temperature dependent constant
ε_∞	the optical frequency dielectric constant
ω_{TO}	the zone-center transverse optic mode frequencies
ω_{LO}	the zone-center longitudinal optic mode frequencies
m^*	the effective mass of the electron
d_{hkl}	interplanar spacing of the planes (hkl)

LIST OF ACRONYMS

Acronyms	Description
AFM	Atomic force microscopy
BTO	Barium titanate, $BaTiO_3$
FWHM	Full width at half maximum
LMBE	Laser molecular beam epitaxy
MBE	Molecular beam epitaixy
PLD	Pulsed laser deposition
RF	Radio frequency
RHEED	Reflection high energy electron diffraction
rms	Root mean square
TEM	Transmission electron microscopy
STO	Strontium titanate, $SrTiO_3$
UHV	Ultra-high vacuum
XRD	X-ray diffractions
YBCO	$YBa_2Cu_3O_y$

CHAPTER 1

INTRODUCTION

1.1 The Origin of Ferroelectricity

Ferroelectric is an insulating system which exhibits spontaneous electric polarization, and the direction of which can be switched between at least two discrete stable or meta-stable states with an applied electric field [M. E. Lines, 1977]. After first observed by Valasek in 1920, in the Rochelle salt ($NaKC_4H_4O_6 \cdot 4H_2O$), ferroelectricity has been found to exist in over three thousand kinds of natural and manufactured compounds. Nowadays, many of the ferroelectric materials have found applications in the electrical and electronic industries. During the past two decades, revolutionary breakthroughs have occurred in understanding ferroelectric materials, both from theory and experiment areas. First principle approaches have allowed precise, quantitative predictions of material properties, including the Berry-phase formulation of ferroelectricity [A. Shapere, 1989; R. Resta, 2000]. High quality single crystalline thin films are now available for both fundamental studies and device applications. The need for high dielectric constant insulators and non-volatile memories has motivated the investigation of these materials.

In ferroelectric materials, spontaneous polarization arises from the noncentrosymmetric arrangement of constituent ions and their corresponding electrons in the crystal structure. According to the symmetry, crystals can be divided into the 32 point groups, 11 of them are being centro-symmetric (non-polar), so they cannot exhibit ferroelectrics [J. F. Nye, 1957]. The remaining 21 point groups lack a center of symmetry and may have one or more polar axes, which is a pre-requisite for the piezoelectric behavior of the crystal. Among these crystal classes without an inversion center, there are 10 polar groups which possess a unique polar axis: 1(C_1), 2(C_2), m(C_3), mm2(C_{2v}), 3(C_3), 3m(C_{3v}), 4(C_4), 4mm(C_{4v}), 6(C_6) and 6mm(C_{6v}). Such crystals may display spontaneous polarization parallel to the polar axis. The spontaneous polarization is temperature dependent, resulting in the pyrofect. All ferroelectric crystals are belonging to a pyroelectric crystal class and have the additional property that an external field can reverse their spontaneous polarization, the relationship is shown in Figure 1.1. Thus ferroelectric character can not be determined solely from crystallographic characterization. This reversible polarization response manifests itself as a hysteresis loop in the response of polarization to an external electric field which is very similar to the hysteresis loop seen in ferromagnetic materials [G. H. Haertling, 1999; A. J. Moulson, 1997].

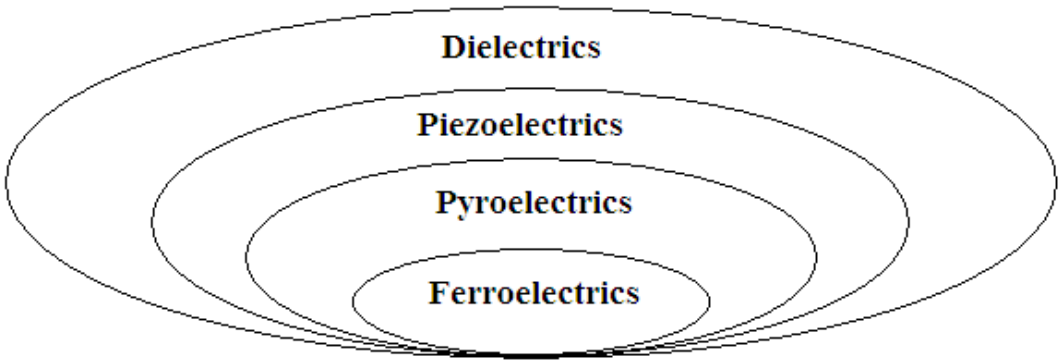

Fig. 1.1 The relationship between dielectrics, piezoelectrics, pyroelectrics and ferroelectrics.

1.2 Introduction to Perovskite Oxides

While ferroelectricity was first found in hydrogen-boned materials, Rochelle salt and subsequently KDP, perovskite oxide $BaTiO_3$ (BTO) discovered in 1949 dramatically changed the physical understanding of this phenomenon. This material is much simpler and nonhydrogen-containing. The relative simplicity of the perovskite structure led to a deeper understanding of the origin of the ferroelectricity.

1.2.1 Structure of Perovskite Titanate

Perovskite oxide is a very large family in terms of composition and has a general formula of ABO_3, where A represents a divalent or a trivalent cation, and B is typically a tetravalent or a trivalent cation. The physical properties of the entire family are extremely diverse, depending on the composition and cationic ordering. They can be

metallic or insulating and exhibit many different types of structural and magnetic order. [N. Sai, 2000; N. W. Schubring, 1992]. For thin films, substrate clamping effect, strain and size effect also have significant influence [V. Nagarajan, 2000; J. H. Chen, 2002; Woo Young Park, 2003]. An ideal perovskite structure, which can be taken as the high-symmetry reference structure and is the structure of the high-temperature paraelectric phase for most ferroelectric perovskite oxides, has space group $Pm\bar{3}m$, with a simple cubic lattice and a basis of 5 atoms. As shown in Figure 1.2(a), if the A atom is taken at the corner of the cube, the B atom is at the center and there is an oxygen at the center of each face; alternatively, if the B atom is taken at the corner, the A atom is at the center and O atoms are located at the midpoint of each edge [P. Ghosez, 2002; L. Eyraud, 1967].

As clearly shown in Fig. 1.2(b), in the perovskite structure, the B atom is at the center of 6 oxygen first neighbors, arranged at the corners of a regular octahedron. The octahedral are linked at their corners into a three dimensional simple cubic network, enclosing large holes that are occupied by A atoms. Each A atoms is surrounded by 12 equidistant O atoms. The oxygen atoms have a lower-symmetry coordination position, is adjacent to 2 B and 4 A atoms.

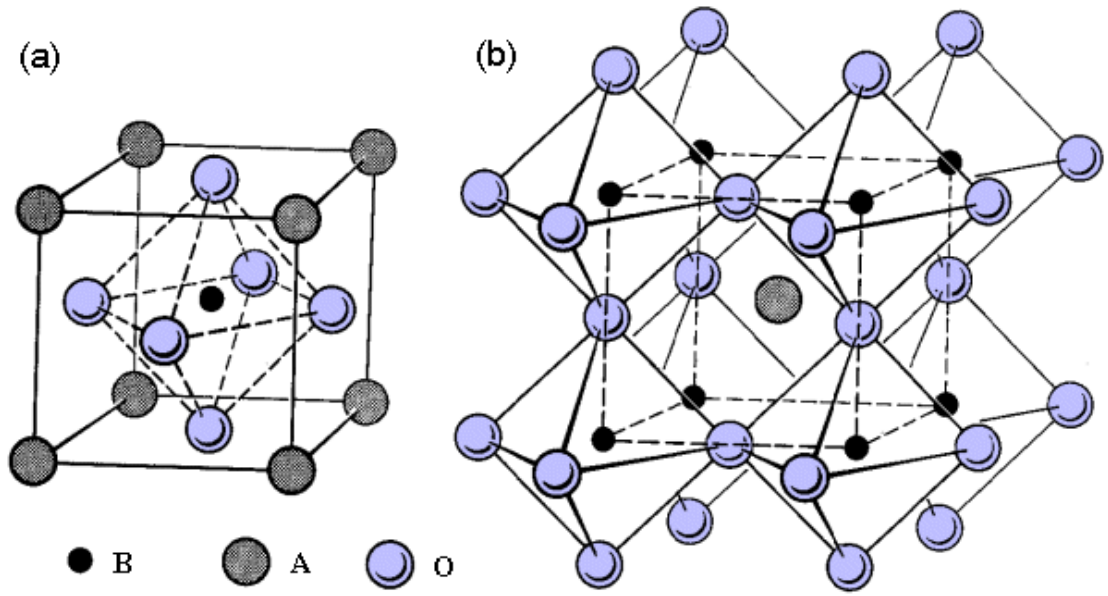

Fig. 1.2 Two different views of the ABO_3 ideal cubic perovskite structure unit cell. The A atom has 12 oxygen first neighbors. The B atom is at the center of an octahedron composed of oxygen atoms.

The prevalence of distortions for compounds crystallizing in the perovskite structured oxide is related to the structural frustration of the cubic perovskite structure regarded as an ionic solid. In 1926, Goldschmidt put forward an empirical model for the stability of the perfect perovskite structure. It is based on the concept of ionic radius and the following two rules: (i) a cation will be surrounded by as many anions as can touch it, but no more; (ii) all the anions must touch the cations and the anion-cation distance is obtained as the sum of their ionic radii. The perovskite structure is fully determined by the size of the oxygen octahedral containing the B atoms, while the A atoms must fit the

holes between the octahedral. In cubic perovskite structure, the ideal relation between ionic radii can be measured through a tolerance factor *t* defined as follows:

$$t = \frac{r_A + r_O}{\sqrt{2}(r_B + r_O)} \quad \text{(1.1)}$$

where r_A, r_B, r_O are the radii of A, B and O atoms, respectively. When t=1, the perfect perovskite structure is formed. When $t > 1$, the structure is imposed by the A-O distance and the B atom is too small for the oxygen octahedron so that the structure will develop a small polar distortion, as in BTO. Conversely, when $t < 1$, the A atom is small in comparison to the hole between the oxygen octahedral, that means the A atom cannot effectively bond with all 12 neighboring O atoms. If *t* is only slightly less than one, rotations and tilting of the oxygen octahedral will be favored, as in $SrTiO_3$ (STO) and $CaTiO_3$.

The metal-oxygen octahedron in the unit cell is believed to be the origin of the ferroelectricity in these materials, and ferroelectricity is directly correlated with the tetragonality of the crystal lattice [R. E. Cohen, 1990]. Take the first perovskite oxide compound BTO as an example, as shown in Figure 1.3. Above the ferroelectric transition temperature, the lattice constant of BTO a = 0.401 nm, so the distance between Ti^{4+} and O^{2-} ions is 0.2005 nm. However, the sum of the Ti^{4+} and O^{2-} ionic radii is:

$$r = r_{Ti^{4+}} + r_{O^{2-}} = 0.064\,\text{nm} + 0.132\,\text{nm}$$

$$= 0.196\ \text{nm}. \quad \text{(1.2)}$$

Obviously, the distance between Ti^{4+} and O^{2-} ions is larger than the sum of the Ti^{4+} and O^{2-} ionic radii, that is, the space of the octahedral interstices is larger than the Ti^{4+} ion. Therefore, the Ti^{4+} ion can move relatively freely inside the oxygen octahedron with very small restoring force. At high temperature, the thermal energy is sufficient to allow the Ti^{4+} ions to move randomly from one position to another, so there is no fixed asymmetry. In this symmetric configuration the material has a paraelectric cubic perovskite structure ($Pm\bar{3}m$). When the temperature is below Curie point, it transforms from a cubic phase to a tetragonal phase (*P4mm*) showing ferroelectric behavior. Each transition is accompanied by small atomic displacements, dominated by displacement of the Ti^{4+} ion relative to the oxygen octahedron [R. E. Cohen, 1992]. As a result, a net-dipole moment in a unit cell forms due to the offset between the mass center of cations and that of anions.

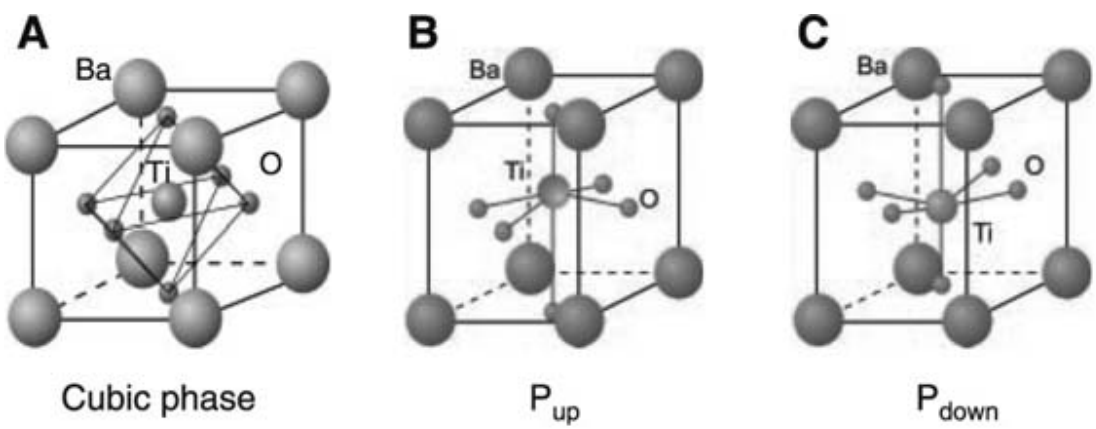

Fig. 1.3 Crystal structures of the perovskite ferroelectric BTO, (A) High-temperature, paraelectric, cubic phase. (B and C) Below Curie temperature, ferroelectric, tetragonal phases, with up and down polarization variants

1.2.2 Curie Temperature

The ferroelectric materials undergo a transformation from a higher crystal symmetry paraelectric phase to a lower crystal symmetry ferroelectric phase when cooled below a certain temperature known as Curie temperature (T_c). The dielectric permittivity rises to a peak at the Curie temperature and above that it decreases according to the well known Curie-Weiss law which is given below:

$$\varepsilon = \varepsilon_0 + C/(T - T_0) \quad (1.3)$$

where ε and C are dielectric permittivity and Curie constant, respectively. T_0 is the Curie-Weiss temperature ($T_0 \leq T_c$), as seen in Figure 1.4. Also, at temperature close to the Curie point, some other thermodynamic properties of the ferroelectric crystal will exhibit large anomalies, such as elastic, optical, and thermal properties. This is called the critical phenomenon.

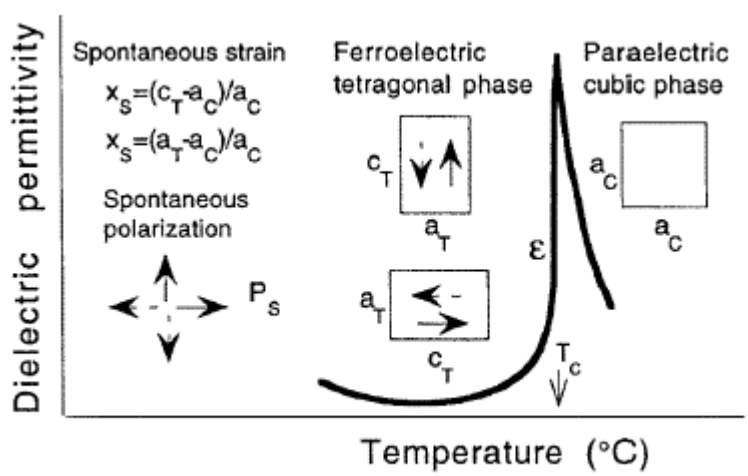

Fig. 1.4 Schematic of ferroelectric material phase transition

1.2.3 Domain

At temperature below T_c, the spontaneous polarization occurs and the crystal structure transforms to lower symmetry, thus causes an increase in the crystal volume leading to a strain in the system. In order to minimize this strain, the system exhibits domain structure. Domains contain uniform alignment of electric dipoles and the boundary between two domains is called the domain wall. Domain walls are characterized by the angle between the directions of polarization on either side of the wall. They can be regarded as abrupt changes in the polarization direction. Figure 1.5 shows the cubic-tetragonal phase transition 180° and 90° domain wall. Generally, domains are formed to reduce the energy of the system. The size and structure of the domains depend on many factors including crystal symmetry, defect structure, magnitude of the spontaneous polarization, grain size, as well as sample geometry and the method of sample preparation [Xu, 1991; Damjanovic, 1998].

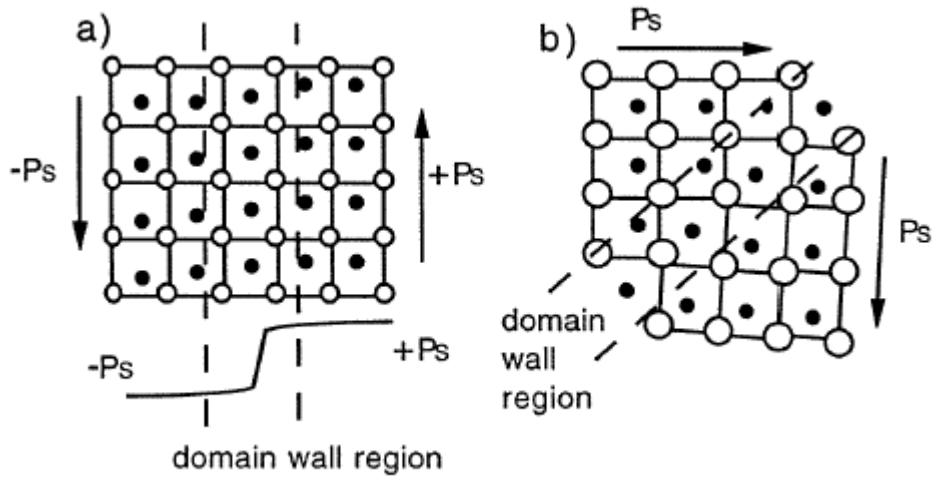

Fig. 1.5 Schematics of ferroelectric domain and domain wall in tetragonal structure perovskite. (a) 180° (b) 90°

1.2.4 Hysteresis Loop

Ferroelectric hysteresis loop (Figure 1.6) is the characteristic of ferroelectric materials, which arises due to the presence of ferroelectric domains in the crystal. When an external dc electric field $E>E_c$ is applied to a poly-domain ferroelectric crystal, it will cause the polarization, *P*, the vectors having different orientations in different domains to align themselves parallel to the direction of the field via domain wall movement. The minimum dc field required to move the domain walls is a measure of the coercive field. The initial value of *Ps* in a polydomain crystal increases with increasing dc field to a maximum that is characteristic of the material. Reversing the electric field reintroduces domain walls movement and results in the Ps in different regions to be reversed. At zero applied field, the crystal will have a remnant polarization which is smaller than the

spontaneous polarization. At fully reversed field, the final *Ps* will have the same magnitude as the original *Ps* but the opposite sign. The hysteretic loop is a function of the work required to displace the domain walls which is closely related to the defect distribution in the crystal and to the energy barrier separating the different orientational states.

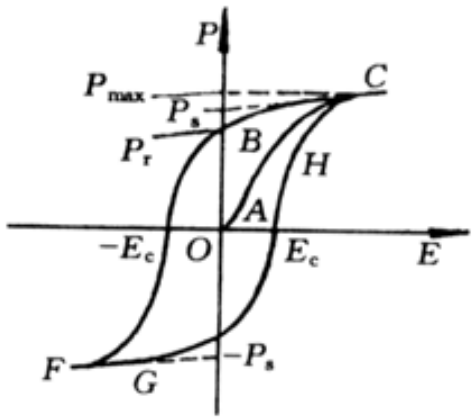

Fig. 1.6 Hysteresis loop showing polarization switching in ferroelectric materials. Important parameters such as coercive field (Ec), remnant polarization (Pr) and saturation polarization (Ps) are indicated in the figure.

1.2.5 Relative Permittivity and Tunability

The ability of ferroelectrics to change their atomic structure while applying an electric field gives rise to extremely high values of permittivity. This is one reason why ferroelectric materials have attracted much interest in their promising potential for a

number of technological application [D. Roy, 1993]. The relative permittivity can be defined in terms of the susceptibility that is directly related to the polarization mechanisms in a material. The real part of the permittivity (ε′) is the dielectric constant and is determined by the magnitude of the polarization. The imaginary component of the permittivity (ε'') is called the loss factor and is governed by the lag in polarization upon application of the field and the energy dissipation associated with charge polarization. It represents the energy loss in a material. This energy loss appears as an attenuation of the applied field and is usually measured relative to the dielectric constant in terms of the loss tangent ($\tan\delta = \varepsilon''/\varepsilon'$). For the frequency and phase agile materials, the critical parameters are a large dielectric nonlinearity and a low microwave loss. To be able to compare the performances of difference devices, a figure of merit

$$K = \frac{\Delta\varepsilon}{\varepsilon \tan\delta_{\varepsilon}} \quad \text{(1.4)}$$

has been introduced. This figure of merit reflects the fact that a tunable microwave circuit can not take full advantage of a high tunability if the loss factor is high. While this figure of merit should be as high as possible, previously reported values have typically been less than 50 [H. N. AL-Shareef, 1997]

Note that dielectric test is often conducted by using an ac signal and the electrical field in the figure actually refers to the field of a dc bias that is applied across the sample under test. It is found that, for a cubic perovskite oxide in paraelectric phase, the ε-E relationship can therefore be written as follows [R. Auer, 1998]:

$$\varepsilon(T,E)=\frac{\varepsilon(T,0)}{\left[1+\left(E/E_0(T)\right)^2\right]^{1/3}} \quad \text{(1.5)}$$

where $\varepsilon(T, E)$ and $\varepsilon(T, 0)$ are the dielectric constant under the electrical field E and zero field, respectively, and $E_0(T)$ is a temperature dependent constant. Thus we see that under an applied external field the denominator in the above equation increases and thus ε decreases as external bias is increased. Thus the dielectric permittivity is maximum at zero bias and goes down with increasing dc bias. Figure 1.7 shows a typical dependence of dielectric constant on electric field.

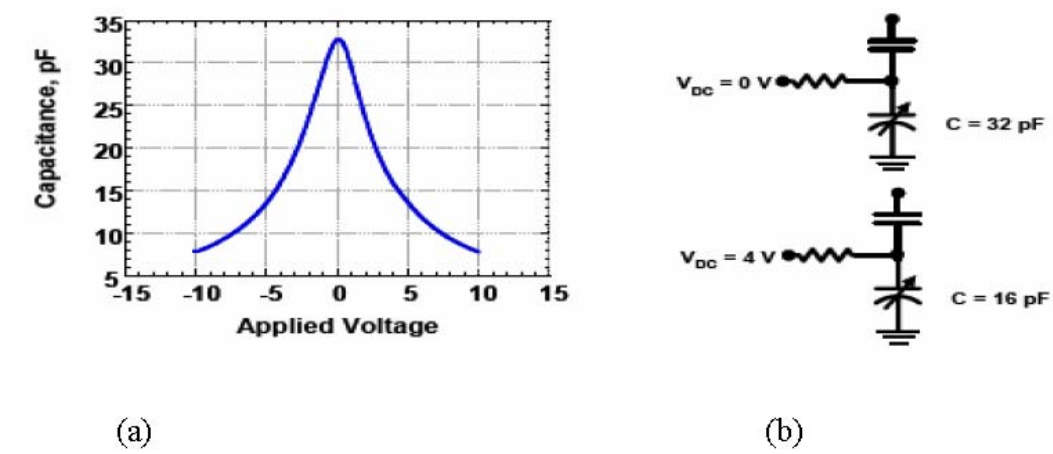

Fig. 1.7 Schematic diagram showing (a) Tunable dielectric behavior of ferroelectric material. (b) Capacitance of a ferroelectric oxide-based capacitor changes as external electric field changes.

The feature of tunable dielectric constant of ferroelectric materials is useful for producing tunable microwave devices. In general, ferroelectric materials are used as

dielectric layers in capacitors. The capacitance of the capacitor is proportional to the dielectric constant of the dielectric material; therefore it can be conveniently changed by changing the voltage applied on the capacitor. Once the capacitance is changed, the impedance and phase of the circuit involving the capacitor is also changed.

1.3 Strontium Titanate

Metal oxides with a perovskite-type structure form a fascinating class of materials, with an extraordinarily varied physics. Among them, STO is a prototype material. STO is a band-gap insulator, with a very large dielectric constant due to the high polarizability of its ionic lattice.

1.3.1 $SrTiO_3$ Single Crystal

In a mechanically free state, bulk STO crystals are cubic perovskite at room temperature, with space group $Pm\bar{3}m$ (O_h^1), but undergo a cubic to tetragonal antiferrodistortive transition below 105 K, with space group $I4/mcm$ (D_{4h}^{18}), which is due to the instability of the zone-corner phonon soft mode and associated with the Ti-O octahedral rotation about a formerly cubic axis [G. Shirane, 1969]. When the energy at the zone boundary reaches zero, the lower symmetry structure condenses. As shown in Figure 1.8(a), the tetragonal structure is still centrosymmetric, hence the phase transition does not lead to ferroelectricity. The other phase transition observed at about 40 K, which is due to the instability of the zone-center soft mode. The Ti ion would shift with

respect to the oxygen ions, as shown in Figure 1.8(b), giving rise to the spontaneous polarization and ferroelectricity. However, the transition is suppressed by quantum fluctuation, thus does not occur. Despite there have a strong softening of the transverse optic polar mode near 0 K, the ferroelectric transition is not occurred in pure STO crystals [R.A. Cowley, 1962]. Therefore, the STO compound is regarded as an incipient ferroelectric, in which the ferroelectric phase transition is suppressed. The quantum mechanical effects in STO has been studied both from theoretical and experimental [E. Tosatti, 1994]. Müller and Burkard first called STO the 'quantum paraelectric' at low temperatures [K.A. Müller, 1979]. At 1991, Müller et al. further proposed that the low temperature state of STO may be a coherent quantum state [K.A. Müller, 1991].

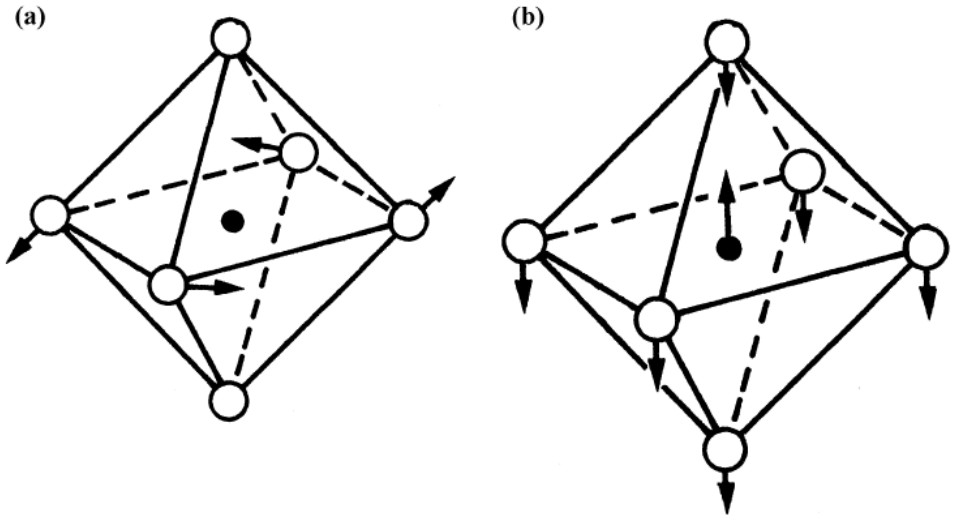

Fig. 1.8 Schematics of the two soft-mode-driven phase transitions in STO single crystal: (a) the cubic-to-tetragonal phase transition at ~105 K, and (b) the ferroelectric phase transition which would occur at ~40 K. The open circles are O ions and the solid circles are Ti ions [X. X. XI, 2000]

The dielectric nonlinearity in STO arises from soft-mode hardening phonon by electric field. The zone-center soft mode frequency in STO single crystal is as a function of temperature and electric field [J.M. Worlock, 1967]: the soft-mode frequency increases when an electric field applied. According to the Lyddane-Sachs-Teller relation,

$$\frac{\varepsilon}{\varepsilon_\infty} = \frac{\omega_{LO}^2}{\omega_{TO}^2} \quad \text{(1.6)}$$

where ε_∞ is the optical frequency dielectric constant, and ω_{TO} and ω_{LO} are the zone-center transverse and longitudinal optic mode frequencies. Higher soft-mode frequency leads to a decrease in the low frequency dielectric constant. The temperature dependence of dielectric constant at different bias electric field was shown in Figure 1.9.

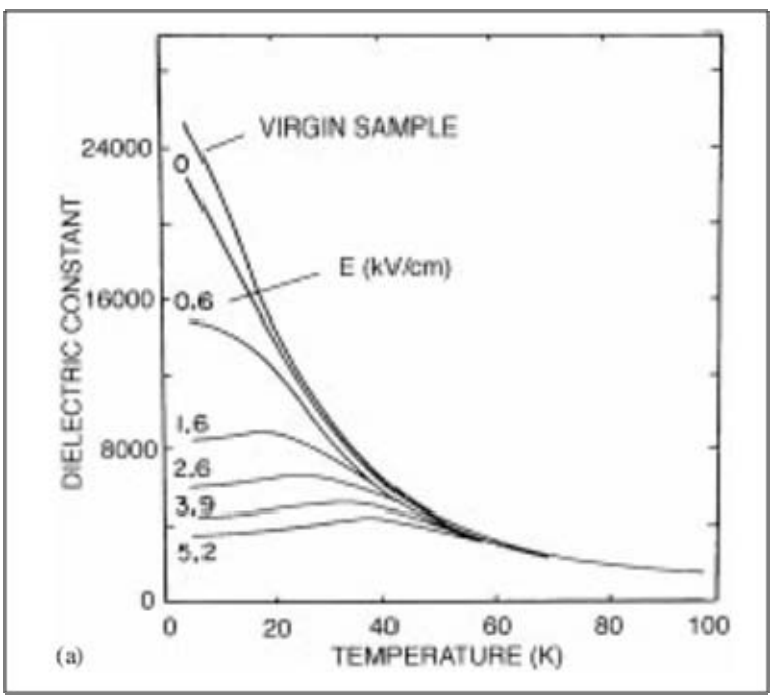

Fig. 1.9 The dielectric constant of a single crystal STO versus temperature at different bias electric field [M. A. Saifi, 1970]

1.3.2 $SrTiO_3$ Thin Films

In the past few years, the study of STO thin films has stimulated interest in exploiting their attractive physical properties for applications. The integration of STO thin films with high temperature superconductor enables potential applications such as resonators, filters, and phase shifters [V. K. Varadan, 1992; R. W. Babbit, 1992; D. Galt, 1993; F. A. Miranda, 1995; C. H. Mueller, 1997]. The integration of STO thin films with semiconductor can find many high impact applications such as metal-ferroelectric-semiconductor field transistors, integrated microelectromechanical systems and ferroelectric random access memories [H. Ishiwara, 1997; D. L. Polla, 1996; O. Auciello, 1998]. Obviously, property of tunable dielectric constant and small loss tangent of STO is a key reason that makes STO useful for a variety of applications.

A wide variety of techniques have been used for the deposition of STO thin films, including pulsed laser deposition (PLD) [H. Tabata, 1994], chemical solution deposition (CSD) [C. L. Jia, 1998], molecular beam epitaixy (MBE) [T. Tambo, 1998], RF sputtering [K. Abe, 1992] and laser molecular beam epitaxy (L-MBE) [M. Yoshimoto, 1992]. Among them, laser ablation technique has been extensively used to grow films of various ferroelectric oxide materials for years. It is easier to obtain the desired film stoichiometry and high quality thin films can be grown reliably in a shorter time compared to other techniques.

Generally, bulk materials requires kilovolts biasing for tuning, resulting in costly and bulky. In contrast, dielectric properties of dielectric thin film can be altered with relatively small dc biasing voltages. Therefore, thin films could enable the development of small, light weight, tunable microwave components. But the dielectric properties of STO thin films are different from those of STO single crystals. Figure 1.10 shows the dielectric constants and loss for an STO single crystal and a thin film as a function of temperature. The loss tangent is plotted as the inset. Typically, bulk form STO has an order of magnitude higher dielectric constant value as well as an order of magnitude lower loss tangent compared to the thin films.

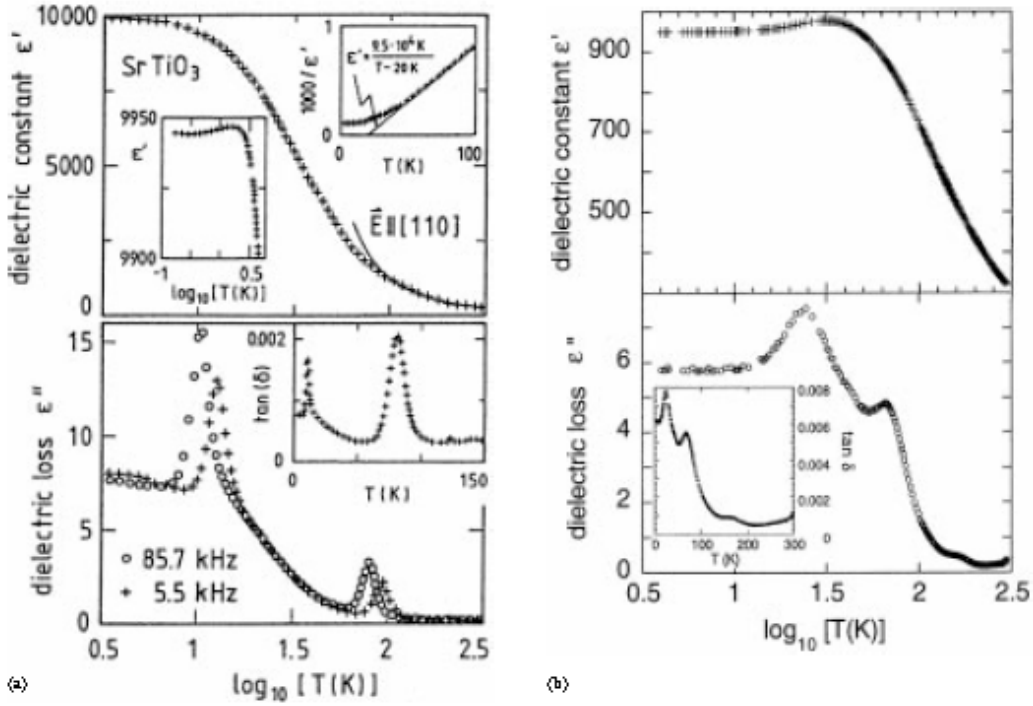

Fig. 1.10 The dielectric constant for (a) an single crystal and (b) an STO thin films as a function of temperature [R. Viana, 1994; X. X. Xi, 2000].

Based on some literature, the reasons responsible for the above difference of STO thin films and bulk can be roughly outline as following:

(1) Substrate has significant influence on the structure and physical properties of STO thin films. In STO single crystal, the ferroelectric state can be induced under pressure [H. Uwe, 1976], applied electric fields [J. Hemberger, 1996], doping impurities [J. G. Bednorz, 1984; C. Ang, 1999], isotopic substitution [M. Itoh, 1999], or the application of stress [A. F. Devonshire, 1954]. All results indicate that this phase transition is sensitive to lattice strain. Therefore, studying the properties of STO thin films under stress will be helpful to better understanding of the ferroelectric phase transitions in related systems. The above considerations motivated some groups to develop a thermodynamic theory of STO epitaxial thin films [N. A. Pertsev, 2000]. Figure 1.11 shows the predicted shift in T_c for STO under biaxial strain. Following this calculation, Haeni *et al.* have reported room-temperature ferroelectricity in strained STO grown on $DyScO_3$ [J. H. Haeni, 2004].

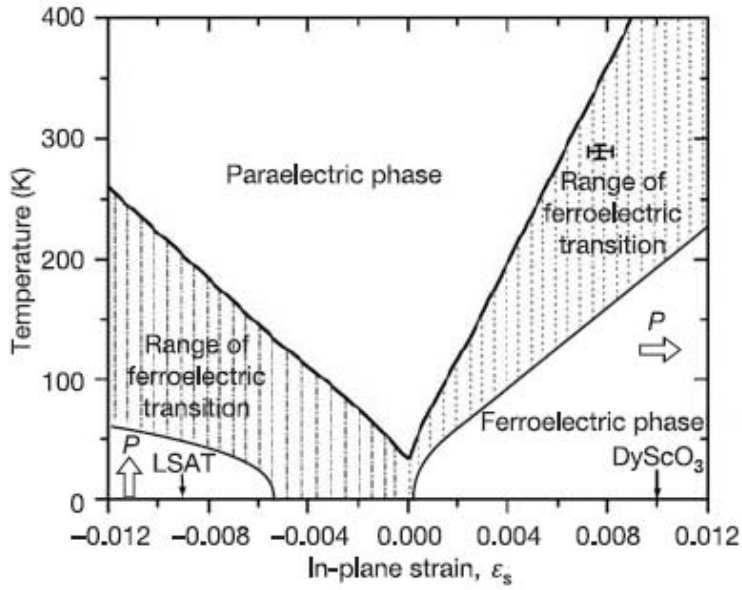

Fig. 1.11 Expected shift in T_c of (100) STO with biaxial in-plane strain, based on thermodynamic analysis [J. H. Haeni, 2004].

(2) The local lattice distortions in STO films also contribute to the lowering of the crystal symmetry, oxygen vacancy is the main defect structure in perovskite titanate [52R. Waser, 1993]. STO thin film can be changed from an insulator to a n-type semiconductor by introducing oxygen vacancy [N. Shanthi, 1998; Z. Luo, 2007]. Various approaches to reduce oxygen vacancies in the ferroelectric insulating thin films have been investigated, such as post annealing in oxygen, use of more active oxygenates, etc.

(3) Interfaces between ferroelectric thin films and electrodes also affect the measured dielectric properties. Some groups have reported reduction of ε results from

an existence of interfacial "dead layer" with poor dielectric properties [C. Zhou, 1997; C. Basceri, 1997]. The phenomena of observed low ε may arise from the oxygen interdiffusion, chemical reaction, structural defects, or Schottky barriers at the interfaces. Thus, an epitaxial growth of thin film with low defect is needed.

1.4 Scope of the Present Study

As discussed above, STO thin film has been extensively investigated, but there are still some questions that remain unanswered. The dielectric properties of STO thin films differ from those in corresponding single crystals and depend crucially on the film quality. Different deposition techniques also affect largely the properties of STO thin films. Thus, a comprehensive understanding of the thin film growth mode is needed. STO thin films can be used as a potential material for tunable microwave devices. One research direction is the combination of STO thin films with high-T_c superconductors, enabling frequency tunable resonators and filters to operate in GHz regime. Thus, the fabrication of high quality STO/$YBa_2Cu_3O_y$ (YBCO) heterostructure is the first step towards novel tunable microwave devices. On the other hand, the fabrication of microwave device from STO-based thin films requires appropriate substrates for both mechanical support and device integration. For tunable microwave applications, an appropriate substrate must have low insertion loss. The substrate must be large area, low cost, thermally stable, and must not perturb the performance of the active layers constituents of the device. The integration of STO with Si has been extensively studied. However, Si is not a "microwave friendly" material, i.e., at microwave frequencies, Si

becomes less resistive, and consequently is too lossy for use in microwave devices. Therefore, Si is not the semiconductor of choice for microwave components [R. E. Williams, 1984]. Compared to Si, GaAs has a higher saturated electron velocity and higher electron mobility. Furthermore, transistors made from GaAs could function at much higher frequencies at very low power-supply voltages. Unfortunately, epitaxial growth of STO thin film on GaAs is difficult due to structural incompatibility and interdiffusion between GaAs and STO.

The main objective of this thesis is to study the growth process, resultant structural properties, and dielectric properties of perovskite titanate thin films.

A short literature review is given in this Chapter, including the introduction to ferroelectricity, perovskite oxides and STO material.

Chapter 2 gives a short introduction to key techniques that have been employed in the study, including L-MBE for thin film deposition, reflection high energy electron diffraction for *in-situ* monitor the growth mode, X-ray diffraction for the determination of crystal structure of thin film, atomic force microscopy, Raman spectroscopy, transmission electron microscopy and dielectric property measurements.

Chapter 3 focuses on the fabrication of STO/YBCO multilayers on different substrates by L-MBE. Microstructure, lattice dynamic and dielectric properties of the multilayers have also been investigated.

Chapter 4 focuses on the integration of perovskite thin film STO on GaAs substrate by L-MBE. Integration of BTO with GaAs using STO as a buffer layer was investigated.

Conclusions and suggestions for future work are given in Chapter 5.

1.5 Statement of Original Contributions

The original contributions of the work presented in this thesis are summarized as follows:

1. The heterostructure of STO/YBCO/$LaAlO_3$ and STO/YBCO/STO was deposited using L-MBE technique. The growth mode and dielectric properties of these structures are also studied.

2. Epitaxial STO films were grown on GaAs (001) substrates without any buffer layers using L-MBE. Studies of the microstructure and dielectric properties of these STO/GaAs heteroepitaxial structure are also presented

3. The heterostructure of BTO/STO/GaAs was fabricated using O_2 flowing L-MBE technique. Ferroelectric properties and transport characteristics of the perovskite titanates/GaAs heterostructure are demonstrated.

CHAPTER 2

DEPOSITION AND CHARATERIZATION OF PEROVSKITE TITANATE THIN FILMS

2.1 Introduction

The study of perovskite titanate thin films involves a number of advanced techniques and facilities for the growth and characterization of thin films. They include:

(1) Thin film deposition and electrode patterning: pulsed laser deposition (PLD), laser molecular beam epitaxy (L-MBE), magnetron sputtering

(2) Structural characterization of thin films: Reflection high energy electron diffraction (RHEED), X-ray diffraction (XRD), Atomic force microscopy (AFM), Raman spectroscopy, Transmission electron microscopy (TEM).

(3) Electrical characterization: dielectric tests by impedance analyzer, ferroelectric tester and leakage current measurement.

In this chapter, a short introduction is given to these techniques that are particularly used in our research.

2.2 Laser Molecular Beam Epitaxy

In this study, perovskite titanate thin films are required to be chemically stoichiometric and epitaxially aligned on substrates. In order to achieve well control thin film in terms of composition and quality, we chose PLD and L-MBE as major techniques for the deposition of thin films. L-MBE is developed from the PLD, therefore we only give a short introduction to the L-MBE method in this chapter.

A wide variety of techniques were employed to fabricate high quality titanate thin films. As a primarily important technology, molecular beam epitaxy (MBE) enable atomic control and characterization of thin film growth process of semiconductor. On the other hand, the discovery of high-T_c superconductivity stimulated the progress in the fabrication technology of thin films of complex oxides. Among many methods, PLD was verified to be especially useful for transforming sintered targets of cuprate superconductors into thin films for electronic device application. Advantages of PLD exist in the deposition under relatively high oxygen pressure, which was favorable for controlling volatile oxygen content in the film, and in the preservation of target composition in the film. Based on these, some researchers have attempted to combine the advantages of both MBE and PLD deposition technology. In 1983, J. H. Cheung et al. replaced a molecular flux source to the solid target in a traditional MBE system [J. H.

Cheung, 1983]. In 1991, M. Kanai et al. had attempted the thin film form by the laser ablation method under molecular beam epitaxy equipment condition [M. Kanai, 1991]. Therefore, a new powerful tool has been added for preparing thin film materials.

The photograph and schematic diagram of the L-MBE system used in our laboratory are shown in Figure 2.1 (a) and Figure 2.1 (b), respectively. The basic components of a LMBE system include: (1) Pre-loading chamber, (2) Ultra-high vacuum (UHV) chamber; (3) RHEED; (4) Rotating target and substrate holder.

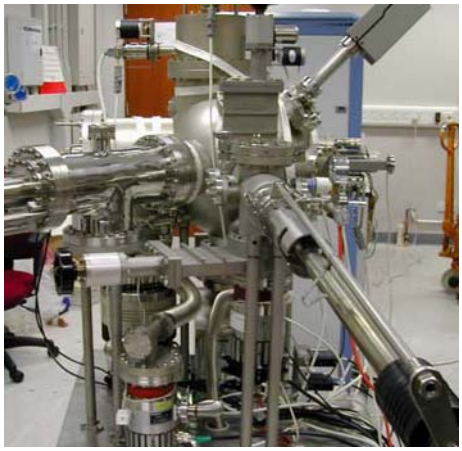

Fig. 2.1 (a) Photograph of our L-MBE system.

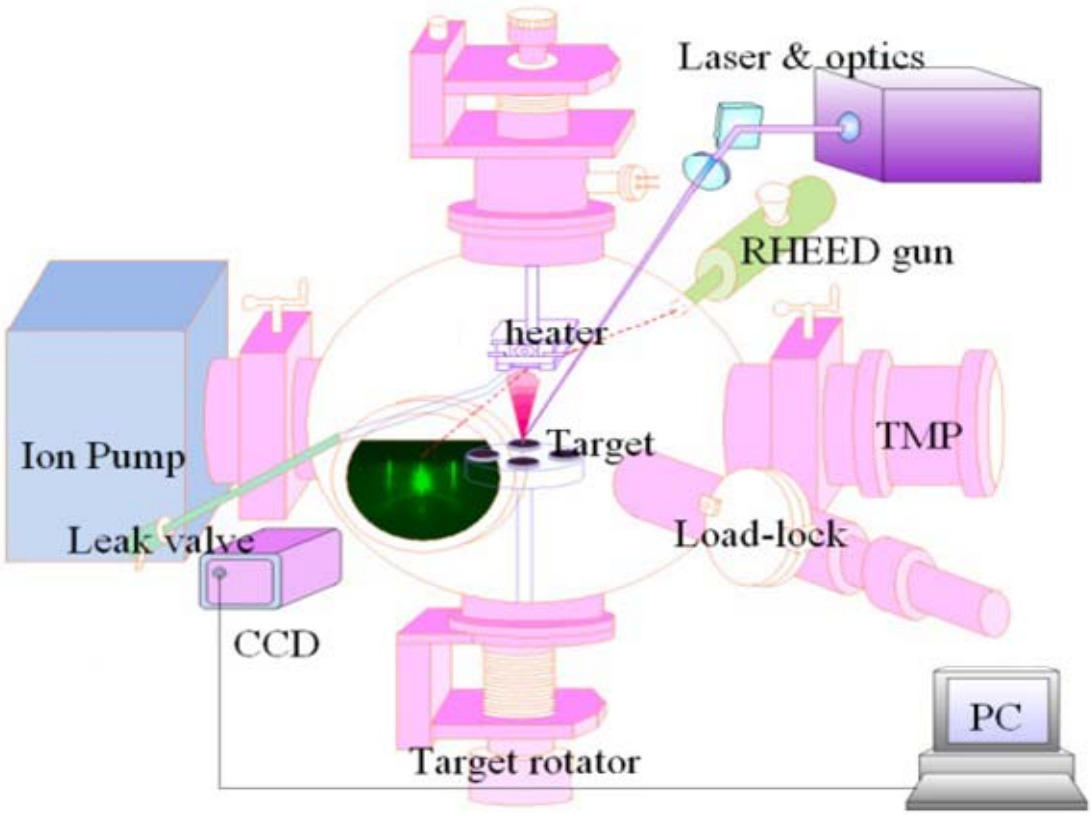

Fig. 2.1 (b) Schematic illustration of the L-MBE system.

The ablation process takes place in an ultra high vacuum chamber - either in vacuum without inserting reactive gas or in the presence of some reactive gas. In the case of oxide films, oxygen is the most common reactive gas for the deposition of oxides. During the deposition, RHEED was employed to characterize the surface of crystalline thin film and *in-situ* monitoring the growth mode during the deposition.

LMBE is one kind of physical vapor deposition, involves complex physical phenomena such as collisional, thermal, and electronic excitation, exfoliation and hydrodynamics etc. Generally, it can be divided into the following three steps:

1. Laser radiation interaction with the target surface.

A KrF excimer laser with a wavelength of 248 nm and pulse duration of 25 ns (Lambda Physik COMPex 205) is focused onto a metallic or ceramic target by a lens external to the chamber. The surface layer material of the target is evaporated when the laser energy density (energy per unit area at the target surface) is above a threshold value, forming a plasma plume with high energetic species. Multiple targets can be used during the deposition process, enabling the growth of a multilayered film.

2. Dynamic of the ablation materials

The material evaporated from the target is highly energized and consists of exited and ionized species forming the plasma. The plasma expands away from the target with a strongly forward-directed trajectory toward a heated substrate placed directly in the line of the plume.

3. Nucleation and growth of a thin film on the substrate surface

The dissociated energetic species impinge onto the substrate surface and the mechanism of the interaction is illustrated in Fig. 2.2. An equilibrium is established between the incoming and re-evaporating species depending on the rate of the particles and substrate temperature, which in turn determines the film growth rate. The crystalline

film growth depends on the surface diffusion of the atoms. Normally, the atom will diffuse through several atomic distances before sticking to a stable position within the newly formed film. High temperature gives atom high mobility which resulting in rapid and defect free crystal growth, whereas a crystal growth at low temperatures or large super-saturations may be dominated by the energetic particle impingement, resulting in disordered or even amorphous structures.

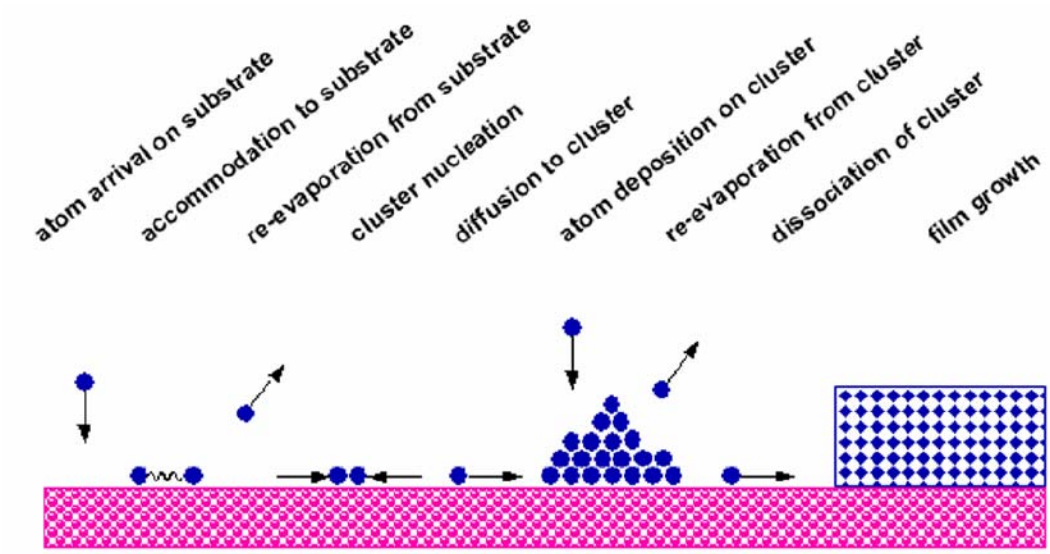

Fig. 2.2 Schematic of nucleation and growth of crystals on a substrate

Each stage in L-MBE deposition is critical to the formation of high quality thin film in terms of epitaxy, stoichiometry, and surface roughness. During deposition parameters are optimized to achieve high quality film growth. These include substrate temperature, laser energy density and frequency, target-to-substrate distance, base

pressure and deposition gas pressure etc. The substrate temperature is critical to the crystallinity of the films. Normally, an amorphous phase forms when the substrate temperature is below a certain value. As the substrate temperature increases films start to crystallize. To achieve an epitaxial growth, the substrate temperature should be optimized, which is different for different materials. The energy density of the laser beam has significant effects on the uniformity of the film. Target-to-substrate distance is a parameter that governs the angular spread of the ablated materials. The oxygen partial pressure is also a very important parameter in the growth of oxide films. The chamber is normally pumped down to a base pressure of ~1 x 10^{-5} Pa before the reactive gas, such as oxygen, is introduced into the chamber.

2.3 Structural Characterization

2.3.1 Reflection High Energy Electron Diffraction

Reflection high-energy electron diffraction has become an important tool in surface science because of its high surface sensitivity. It utilizes diffraction of electrons by surface atoms and provides information of the periodic arrangement of the surface atoms. Because of the compatibility with ultra high vacuum deposition techniques, it is often used for the investigation of the surface morphology during thin film growth. A typical RHEED measurement system consists of an electron gun, a phosphor screen and image-processing hardware and software. Multi-stage diffusion pump was used in our L-

MBE system to keep high vacuum for the electron gun. Thus the RHEED can *in-situ* monitor the oxides deposition under a relatively high oxygen pressure in main chamber.

2.3.1.1 Geometry and Basic Principles of RHEED

A schematic drawing of a typical RHEED geometry is sketched in Fig. 2.3. The electron beam strikes the sample surface at a grazing angle θ_i (0.1^o~5°). The electron energy used in our RHEED is 30 K*eV*. The corresponding amplitude of the wavevector k_0 for these high-energy electrons can be estimated using:

$$E = \sqrt{\frac{\hbar^2 |k_0|^2}{m^*}} \quad \text{(2.1)}$$

where E and m^* are the electron beam energy and the effective mass of the electron, respectively. Without relativistic correction the electron wavelength λ can be estimated by:

$$\lambda = \sqrt{\frac{150}{E}} \quad \text{(2.2)}$$

In the case of electron beam energy in our RHEED system is given in 30 K*eV*, the electron wave λ is calculated as about 0.0707 Å, which is an order of magnitude smaller than the thickness of an atomic layer. For the glancing incidence angle is less than 5°, RHEED only samples a few atomic layers beneath the surface, the periodic part of the crystal beneath the surface can be neglected, which makes RHEED a surface sensitive diffraction technique.

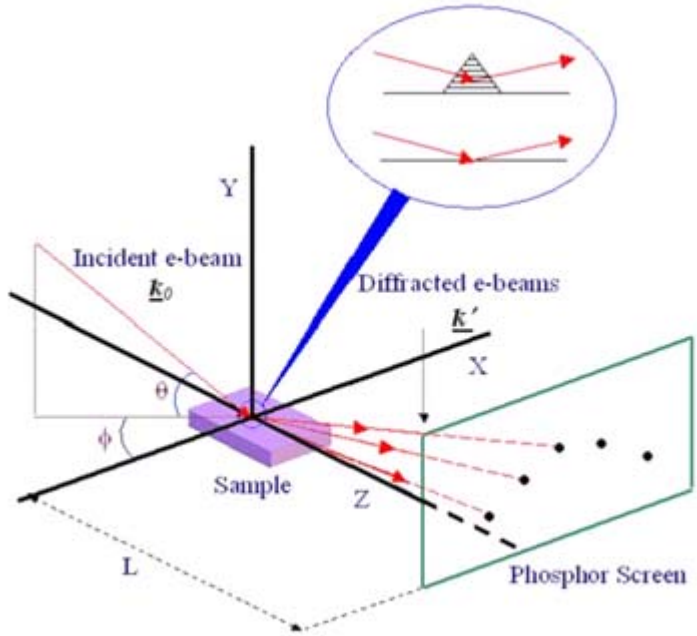

Fig. 2.3 Schematic view of the RHEED geometry.

The electron gun and phosphor screen are located far from the sample to avoid interference with the deposition process. In this geometry, electrons are scattered from the crystal surface resulting in a characteristic diffraction pattern on the phosphor screen. This pattern is instantaneously displayed and can be used to define the crystallographic surface structure.

The surface diffraction observed using RHEED is an image of the reciprocal lattice of the surface structure. Then the kinematical scattering theory is used to describe RHEED diffraction. The diffraction spots are produced when the momentum of the incident beam and that of the diffracted beam differ by a reciprocal lattice vector *G:*

$$k_s - k_0 = G \quad \text{(2.3)}$$

where k_s and k_o are the wave vectors of the diffracted and incident beams. A useful geometrical representation of the conditions for diffraction in elastic scattering, is provided by the Ewald sphere construction, depicted in Figure 2.4.

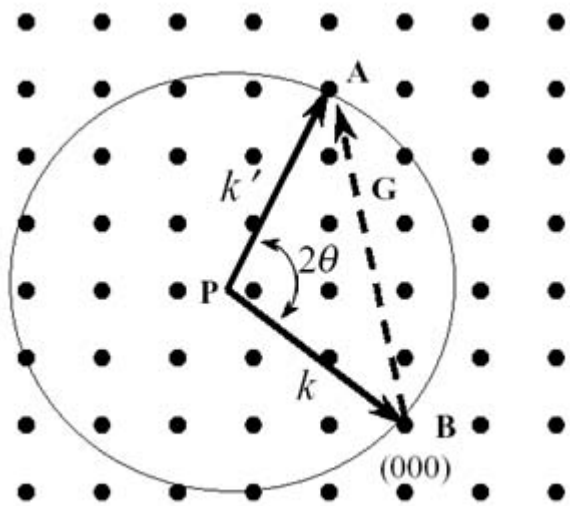

Fig. 2.4 Ewald sphere construction

Since the incident electron energy is very high, the Ewald sphere is quite large compared to the reciprocal lattice spacing of oxide crystals. As a result, only a few reciprocal lattice rods are intersected at the small grazing incident angle. Other areas of the reciprocal space are mapped by rotation of the sample about the incident angle.

For an atomically flat and single domain crystalline surface, the rods are narrow, and spots are observed along an arc on the RHEED screen where the inplane momentum

transfer of the scattered electrons has the value of the reciprocal lattice. If broad rods or streaks are observed, this is due to poor crystallinity where the rows of atoms are partially disordered and are arranged with a range of angles relative to the incident beam.

2.3.1.2 Growth Mode

The thermodynamic approach to crystal growth is used to determine growth modes of thin films. Generally the growth modes of thin films are classified into the following four categories, depending on the surface mobility during growth [T. Frey, 1994]. Figure 2.5 shows the schematic description of the various growth modes.

(a) Figure 2.5(a) shows two dimensional (2D) layer-by-layer growth (Frank-van der Merwe growth mode). Layer-by-layer growth is attained with high surface mobility, in which the nucleation of 2D islands and completion of the unit-cell layer proceed in a cyclic manner. In a strict sense, the growth of a second unit-cell layer does not start until the first unit-cell layer is completed. The RHEED specular beam intensity oscillates periodically in time with no damping in amplitude.

(b) Figure 2.5(b) shows three dimensional (3D) island growth (Volmer-Weber mode). Low surface mobility and high supersaturation enable the 3D island growth. In this case, there is no RHEED intensity oscillation. Furthermore, transmission electron diffraction through 3D island gives rise to spotty RHEED patterns.

(c) Figure 2.5(c) shows switching from 2D to 3D growth (Stranski-Krastanov growth mode, SK mode). In this growth mode, initial 2D layer-by-layer growth is switched to 3D island growth after a few atomic layers. In this case, very few RHEED intensity oscillations were observed with damping in its amplitude.

(d) Figure 2.5(d) shows the step-flow growth. If the surface mobility becomes still higher, and the surface diffusion length l_D is larger than the substrate terrace width l_T, then surface steps on the substrate surface will be energetically favorable sites for nucleation. The step density, after the initial film growth, will reach a steady state, giving rise a constant RHEED intensity as a function of time.

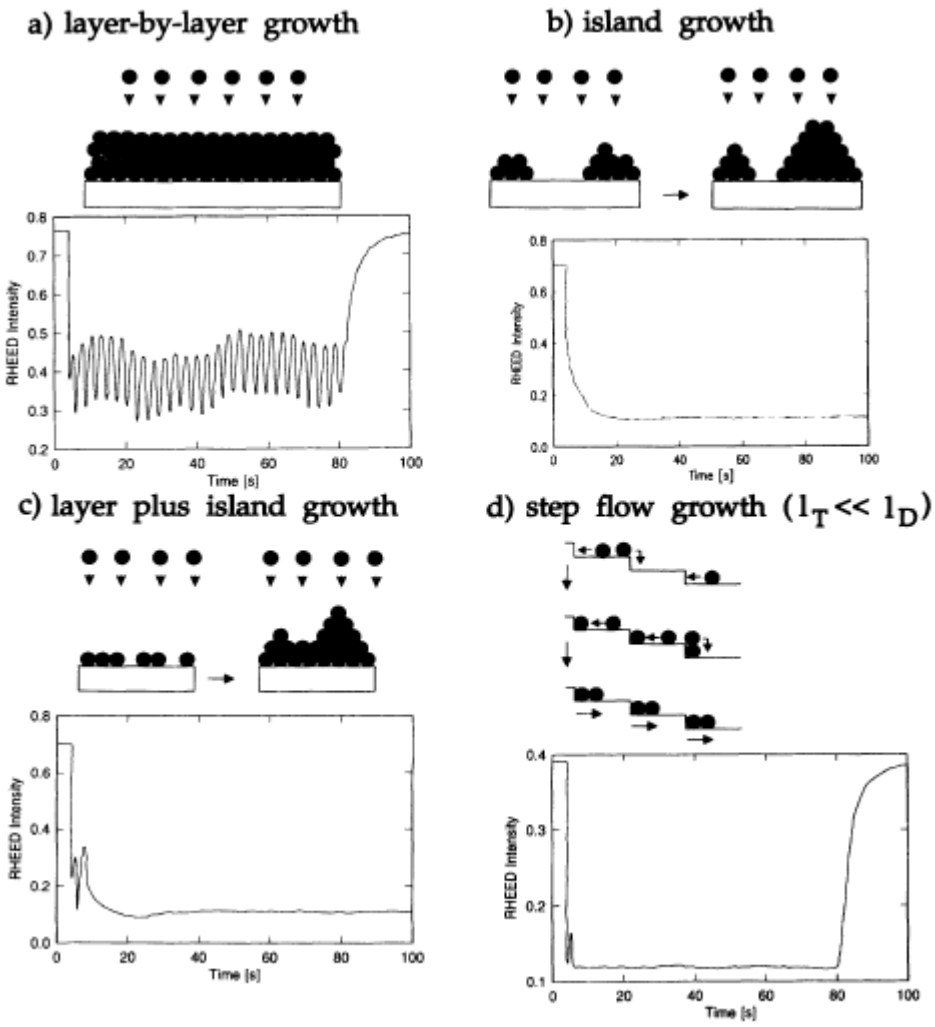

Fig. 2.5 Schematic description of the various growth modes. (a) layer-by-layer growth, (b) island growth, (c) SK growth, (D) step flow growth [T. Frey, 1994].

The property of the thin film is curiously depending on the growth mode. Lippmaa et al. reported dramatically improved dielectric properties of STO thin film which can be comparable with the single crystal could be obtained by optimize the

deposition condition, thus change the growth mode, as shown in Figure 2.6 [M. Lippmaa, 1999].

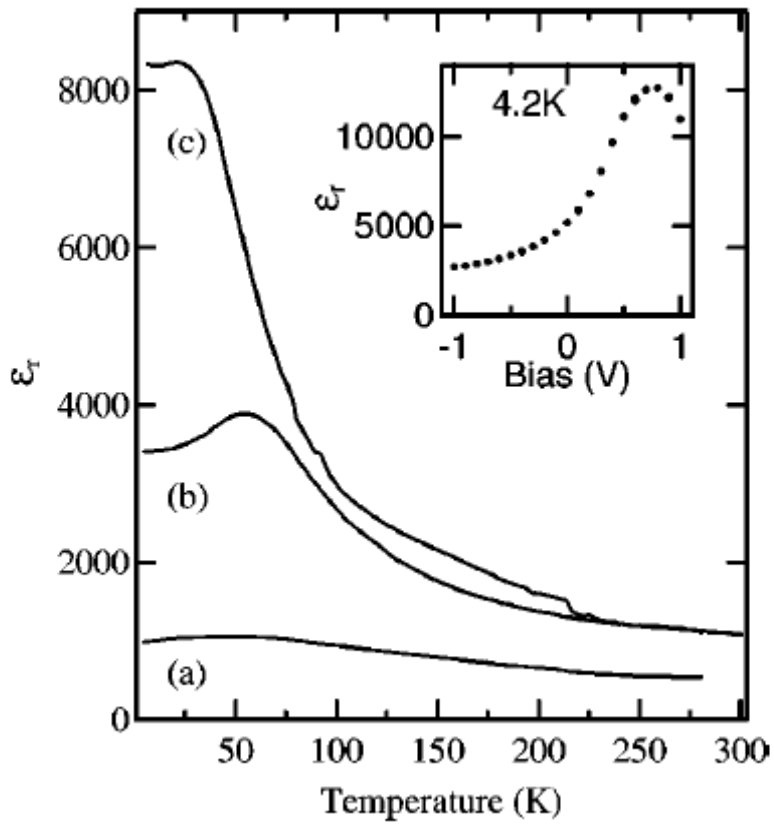

Fig. 2.6 Temperature dependence of the dielectric constant of a film grown in the layer-by-layer mode (a). In the step-flow mode (b). And during heating at a 0.8 V dc bias (c) [M. Lippmaa, 1999].

2.3.2 X-ray Diffraction

X-ray diffraction is a versatile, non-destructive technique to identify the crystalline phases present in solid materials and analyze the structure properties. It is the result of the interaction between X-rays and the periodic electronic potential geometry of crystals. Figure 2.7 shows the basic geometry of XRD. A beam of parallel X-rays impinges on the crystal surface at an angle θ and diffracted at an angle θ. Diffraction occurs as waves interact with a regular structure whose repeat distance is about the same order as the wavelength of the waves. This is expressed in Braggs's Law:

$$2d_{hkl}\sin\theta = \lambda \quad \text{(2.4)}$$

where d_{hkl} is the distance between the lattice planes ($h\ k\ l$) and λ is the wavelength of x-ray beam.

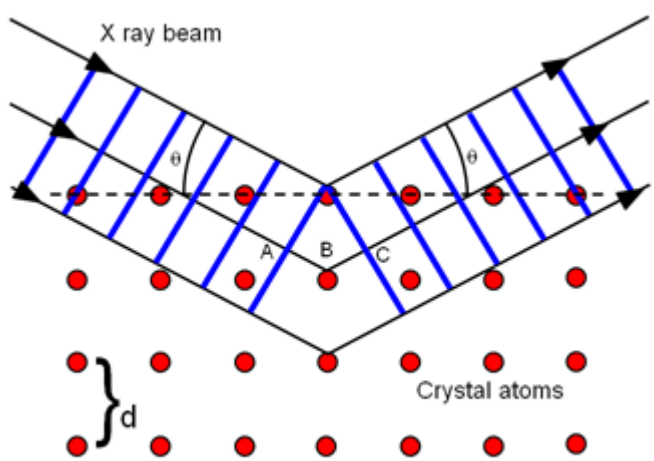

Fig. 2.7 Principle of X-ray diffraction for crystal structure characterization.

The X-ray diffraction measurements were carried out on a Bruker AXS D8 Discover X-ray diffractometer in our laboratory (seen Figure 2.8). The four-circle X-ray

diffractometer is with a horizontal, high-resolution Ω-2θ goniometer. An open Eulerian cradle provides two additional axes of rotation (-90° < ψ < 90°, and -360° < φ < +360°). The X-ray source is a long-fine-focus, ceramic X-ray tube with Cu anode. Normal operating power is 40 kV and 40 mA and Cu Kα radiation with a wavelength λ = 0.15406 nm is used. The sample stage supports monolithic specimens of a wide variety of shapes and sizes. X-ray structural analysis can be used to determine the epitaxial feature of the thin films. The techniques include θ-2θ scans, φ scans, and rocking curves. θ-2θ scans are used to determine the crystalline orientation of the thin films. The full width at half maximum (FWHM) of the resulting peak gives an indication of the degree *c*-axis orientation of the crystal which can be determined with a rocking curve. φ scans can be performed to determine the expitaxy of the films.

Fig. 2.8 Four-circle X-ray diffractometer (Bruker AXS D8 Advance).

2.3.3 Atomic Force Microscopy

Atomic Force Microscopy (AFM) is a non-destructive technique used for characterize the surface topography of the sample. AFM gets information based on the atomic forces between a cantilever and the surface and can image wide range of materials such as insulators, semiconductors and metals [D. P. Woodruff, 1994; M. Miles, 1997]. The first AFM was developed by Binnig et al. in 1986. Commercial AFM began to widely used in the early 1990s [Morris, 1999].

Figure 2.9 shows the major components of an AFM, it contains a tubescanner, a position-sensitive photo-detector, and a cantilever with a probe located at the free end. When the tip brought close to the sample, various interactions are present at the atomic level. The sensed interaction can be correlated to the distance between the tip and sample. The scanner is piezoelectric ceramic which provides the precise positioning control. Piezoelectric ceramic changes its geometry when a voltage is applied. The voltage applied is proportional to the resulting mechanical movement. The piezoelectric scanner is designed to bend, expand, and contract in a controlled, predictable manner. Therefore, it can provide a way of controlling the tip-sample distance and of moving the tip over the surface. Most of the AFM operated by keeping a constant force between the tip and the sample and by moving the sample to provided useful images. However, some investigation shown that there are many other modes by which sharper images can be obtained. There are mainly three types of mode: contact mode, non-contact mode, and

tapping mode. The comparison of these modes can seen from the table 2.1. Our measurements were carried out in the tapping mode to determine surface microstructure, roughness and grain size.

Table 2.1 Comparison of three different contact mode.

Modes	Advantages	Disadvantages
Non-contact	1. No force exerted on the sample surface.	1. Lower lateral resolution. 2. Lower scan speed. 3. Only works on extremely hydrophobic samples.
Contact	1. High scan speeds. 2. Only technique can obtain “atomic resolution” images. 3. More easy to scan the sample with extreme changes in vertical topography.	1. Lateral forces can distort features in the image. 2. The combination of lateral forces and high normal forces can result in resulted spatial resolution and may damage soft samples.
Tapping	1. Higher lateral resolution. 2. Lower forces and less damage to soft samples imaged in air. 3. Lateral forces are virtually eliminated, so there is no scraping.	1. Slow scan speed.

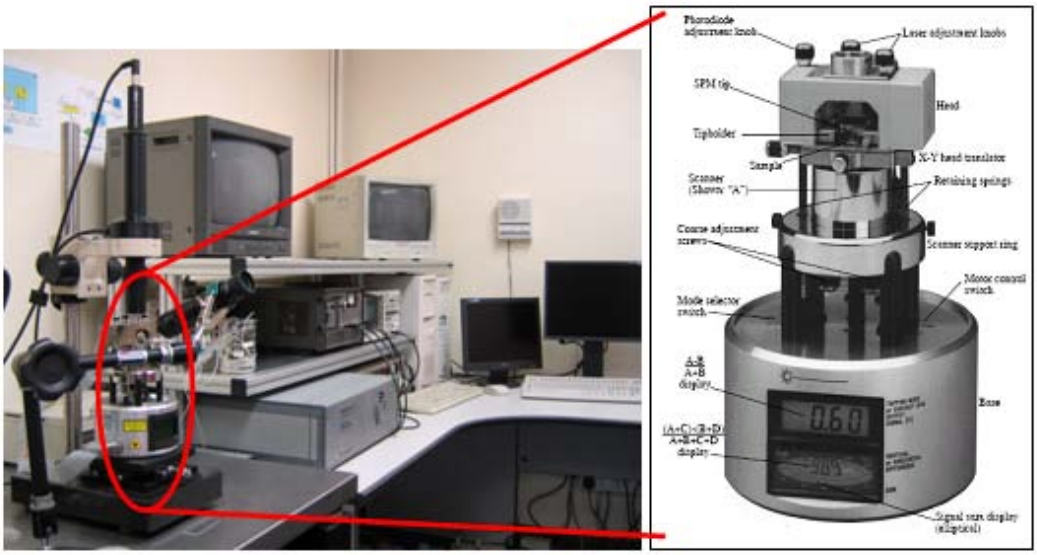

Figure 2.9 The major components of an AFM

2.3.4 Raman Spectroscopy

Raman spectroscopy is a spectroscopic technique used in condenses matter physics and chemistry to study vibrational, rotational, and other low-frequency modes in a system. Raman's effect occurs when laser light is impinges upon materials and the light is scattered. The laser light interacts with phones or other excitations in the system, resulting in the energy of the laser photons being shifted up or down. The shift in energy gives information about the phonon modes in the system, if the wavelength of the scattered radiation is analyzed, both incident radiation wavelengths (elastic scattering) and a relatively small amount of radiation (inelastic scattering) can be determined. Figure 2.10 shows the procession of Raman scattering.

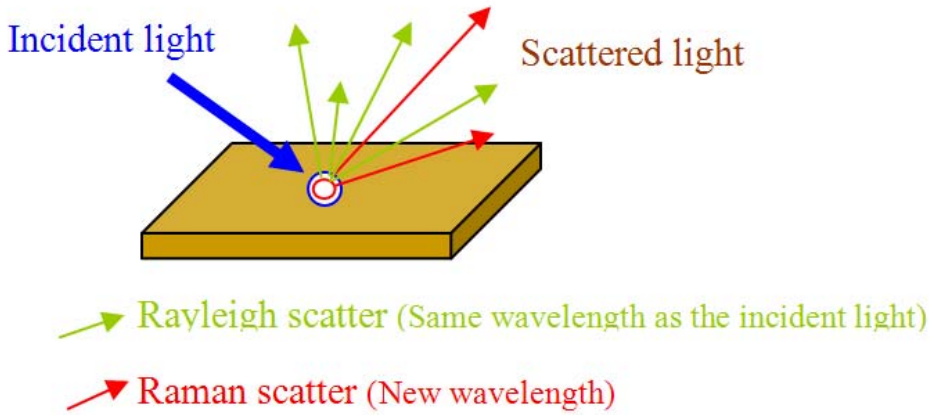

Fig. 2.10 The principle of Raman scattering

There are three kinds of scattered lights in a Raman-experiment, they are stokes which wavelength of the Raman scattered photons λ_s is larger than that of incident λ_i, Rayleigh which is no wavelength changed in the incident λ_i and Raman scattered photons λ_s and anti-stokes which wavelength of the Raman scattered photons λ_s is smaller than that of incident λ_i, and the diagram of them are shown in Figure 2.11

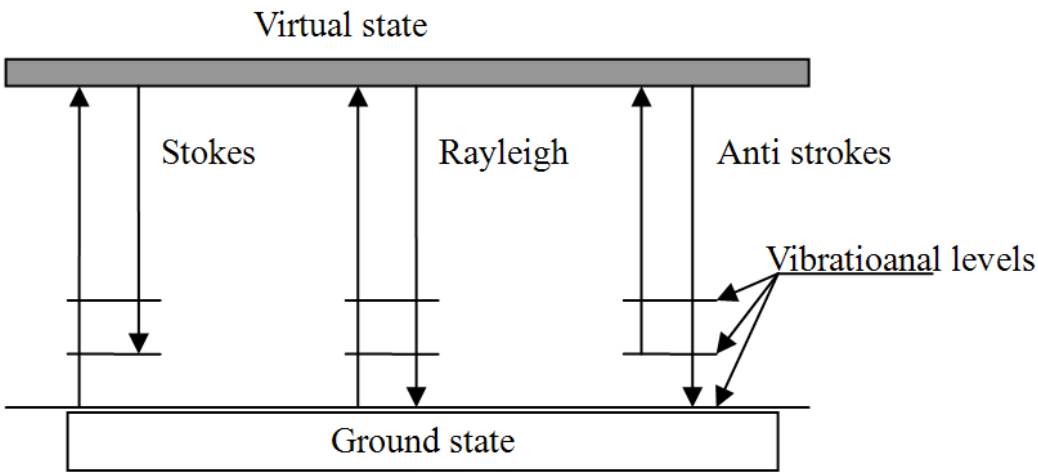

Fig. 2.11 Schematic diagram of three kinds scattering lights

It is the shift in wavelength of the inelastically scattered radiation that provides the chemical and structural information. Raman shifted photons can be of either higher or lower energy, depending upon the vibrational state of the molecule under study. Stokes radiation occurs at lower energy (longer wavelength) than the Rayleigh radiation, and anti-Stokes radiation has greater energy. The energy increase or decrease is related to the vibrational energy levels in the ground electronic state of the molecule, and as such, the observed Raman shift of the Stokes and anti-Stokes features are a direct measure of the vibrational energies of the molecule. The energy of the scattered radiation is less than the incident radiation for the Stokes line and the energy of the scattered radiation is more than the incident radiation for the anti-Stokes line. The energy increase or decrease from the excitation is related to the vibrational energy spacing in the ground electronic state of the molecule and therefore the wavenumber of

the Stokes and anti-Stokes lines are a direct measure of the vibrational energies of the molecule. The relationship of the Raman shift (ν) and the wavelengths in cm of the incident λ_i and Raman scattered photons λ_s can be written as the following equation:

$$\upsilon = \frac{1}{\lambda_i} - \frac{1}{\lambda_s} \quad \text{(2.5)}$$

2.3.5 Transmission Electron Microscopy

Transmission electron microscopy (TEM) is a powerful analytical in materials characterization. The optical principle of TEM is similar to that of the conventional optical microscopy. The only difference is that TEM uses electrons as source, and the electron beam is focused by a series of electromagnetic lenses. In order to characterize a sample by TEM it has to be thinned down to approximately 50 nm, to become sufficiently transparent for electrons. When electrons hit on the sample surface, several reactions would occur, the diffracted beams are then brought to focus by the objective lens on its back focal plane and form a diffraction pattern. The main imaging and diffraction techniques include: 1. Conventional imaging (bright-field and dark-field TEM); 2. Electron diffraction (selected area electron diffraction, SAD); 3. Convergent-beam electron diffraction (CBED); 4. Phase-contrast imaging (high-resolution TEM, HRTEM); 5. Z-contrast imaging. In our labortory, the instrument is a JEOL JEM-2001 TEM operated at 200 kV, with high-resolution, STEM, EDX and other functions (Figure. 2. 12).

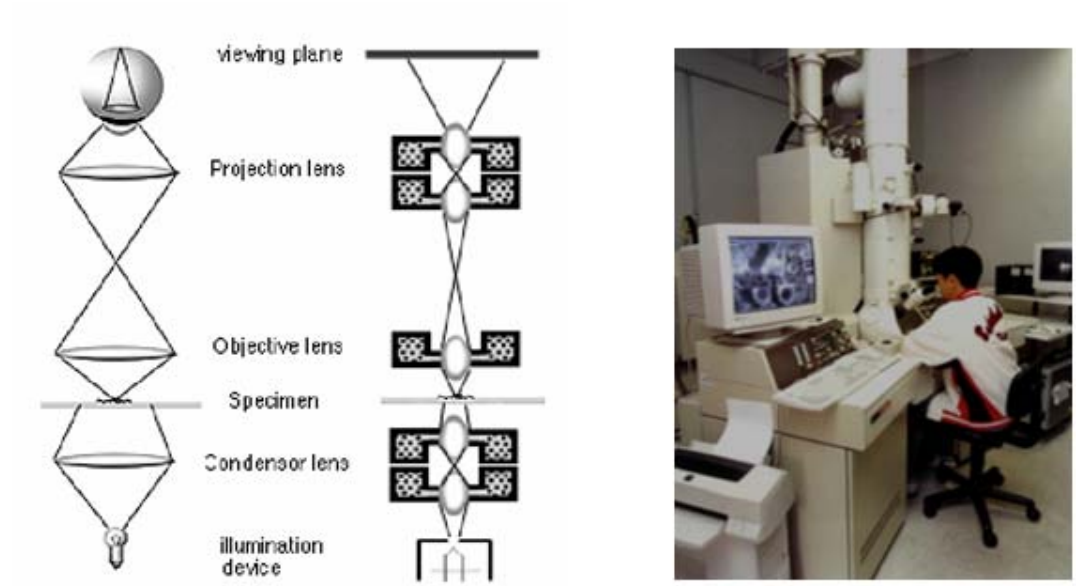

Fig. 2.12 Schematic diagram of TEM

2.4 Dielectric and Ferroelectric Measurement

The ferroelectric tests were carried out on a ferroelectric analyzer (TF-2000, AixACCT Systems GmbH, Germany) equipped with a high-voltage module. The dielectric measurements were carried out on an impedance analyzer (HP4194A, Hewlett Packard). The capacitance was recorded and the dielectric constant was evaluated using:

$$\varepsilon = \frac{Cd}{4\pi\varepsilon_0 A} \quad \text{..... (2.6)}$$

where ε is dielectric constant, ε_0 is the dielectric constant in free space, *C* is the capacitance, *A* is the area of the capacitor and d is the film thickness. A temperature

controller (Cambridge, UK) was employed in the measurements to control the measurement temperature.

2.5 Metal Electrode Deposition

Gold or Platinum thin films as the top electrodes were produced by radio-frequency sputtering and pulsed laser deposition, respectively. Both of which are widely used deposition technique for a variety of metals. The details of the gold and Platinum deposition are given in Table 2.2 and Table 2.3. Thickness of electrode is about 200 nm.

Table 2.2 Deposition conditions for Au sputtering.

Target	Au
dc power	70 W
Substrate temperature	Room temperature
Sputtering gas	Ar (10 sccm)
Gas pressure	35 mTorr
Deposition time	15 min

Table 2.3 PLD deposition conditions for Pt electrode.

Target	Pt
Laser energy density	6 J/cm^2
Frequency	5 Hz
Substrate temperature	Room temperature
Pressure	10^{-3} Pa
Deposition time	20 min

2.6 Summary

In this Chapter, we demonstrated a number of advanced techniques used in the deposition and characterization of perovskite titanate thin films, including L-MBE, RHEED, X-ray diffraction, AFM, Raman spectroscopy, TEM and dielectric and ferroelectric measurement.

CHAPTER 3

STRUCTURE AND DIELECTRIC PROPERTIES OF $SrTiO_3$-$YBa_2Cu_3O_y$ MULTILAYER

3.1 Introduction

In the past few years, the use of perovskite ferroelectric material in microwave devices has been widely investigated. Tuning of the microwave devices can be achieved with either electric or magnetic field. The former depends on the nonlinear ferroelectrics and the latter employs the magnetization nonlinearity of the ferrites [G. F. Dionne, 1997]. The desired properties of the tunable microwave devices are a large tunability and a low insertion loss thus requires the materials possess frequency stable permittivities and low dielectric losses.

For low temperature electronic applications, STO has received great interest due to its high and field-dependent dielectric constant [X. X. Xi, 2000; W. Chang, 2005]. The T_c and the dielectric properties of thin films can be quite different from those in corresponding single crystals. It is believed that the dielectric properties of STO thin films depend crucially on the film quality, determined by film thickness, substrates, interfacial strain, growth modes, *etc* [J. H. Hao, 2000; J. H. Hao, 2006; L. Ryen, 1998;

M. Lippmaa, 1999; V. Vonk, 2004]. Therefore, considerable efforts have been made to grow high quality STO based multilayers with low interface defect and better electronic property. To achieve the goal, it is usual to introduce a lattice- and chemistry-matched perovskite layer, such as high temperature superconductor namely $YBa_2Cu_3O_y$ (YBCO) [R. Ramesh, 1991; R. Ramesh, 1992]. For its surface resistance is more than two orders of magnitude smaller than that of copper at microwave frequencies results in a high quality factor, low loss, sharp skirts, and small size, the YBCO layer can also act as an electrode in STO based multilayer device. Consequently, STO microwave devices introduced YBCO layer are expected to have advantages of both low energy consumption and efficient frequency selectivity, offering attractive options for military, commercial, and space-based communications [T. Van Duzer, 1997], which makes the STO/YBCO bi-layer the most promising for practical low-temperature microwave devices. Figure 3.1 shows two different test designs for ferroelectric capacities for frequency agile microwave resonators.

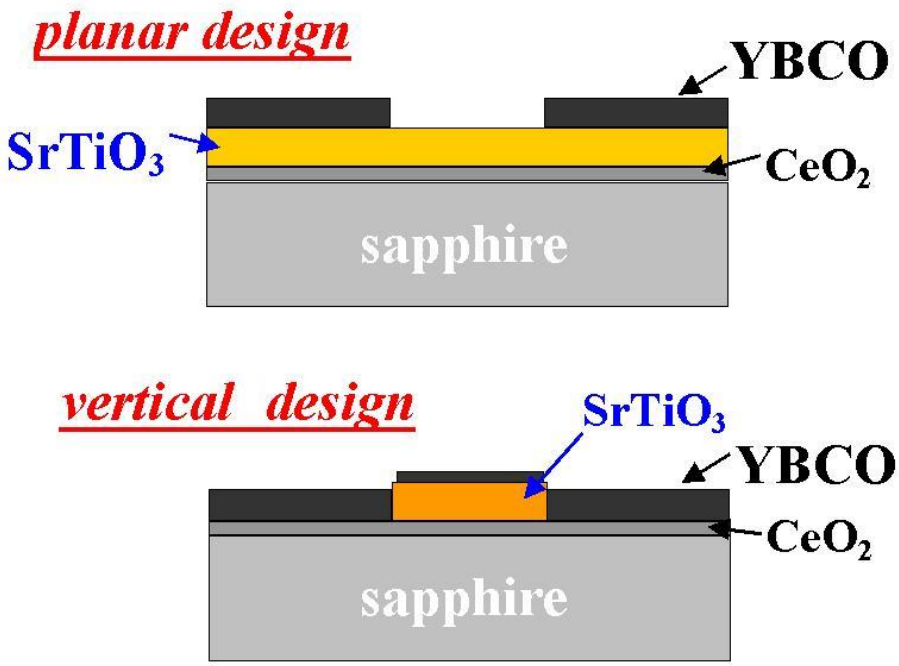

Fig. 3.1 Scematic diagrams of two different designs for ferroelectric capacities for frequency agile microwave resonators [O. Roland, 2002]

However, according to pervious research, the microwave losses measured in STO/YBCO multilayer are significantly higher, has an order of magnitude higher loss tangent than in the STO bulk form. Much research has been focused on the effect of the interface structure on its related electrical properties. A strong temperature dependence of the dielectric properties of $Ba_xSr_{1-x}TiO_3$ thin films on various thickness YBCO layer was observed [X. H. Zhu, 2005]. In previous reports, the growth mode of three-dimensional (3D) spiral-dislocation-mediated island in YBCO thin films was usually

observed. The interface between STO and YBCO becomes rather rough and can alter the dielectric properties of STO thin films on it [M. Hawley, 1991]. Moreover, some groups showed that temperature dependent interface structure and crystal orientation have played an important role in controlling the tunability and other electrical properties [J. S. Wu, 2001; C. Ang, 2001]. Good crystallinity, epitaxial alignment and clean interface are the major requirements for the STO/YBCO multilayer. Therefore, it is much needed to investigate the effect of growth mode in each layer on the preparation of dielectric/superconductor heterostructure, especially at the initial stages, since the microstructural quality near the interfaces is determinant in the transport properties of the devices. In addition, the growth of multilayered heterostructures requires smooth interfaces. With such a well-controlled structure, one may understand the fundamental mechanism responsible for various physical properties.

In this chapter we report our work on the integration of STO/YBCO multilayer by means of the laser molecular beam epitaxy (laser MBE), which combines the advantages of pulsed laser deposition (PLD) and MBE, allowing atomically controlled epitaxy of thin films. We have also investigated microstructure, lattice dynamic and dielectric properties of the multilayers.

3.2 Thin Film Integration and Structure Characterization

3.2.1 Thin Film Deposition by Laser-MBE

STO/YBCO thin films were deposited on $LaAlO_3$ (LAO) and STO substrates by LMBE, respectively. Prior to the deposition, the substrates were *in situ* annealed at the temperature of 800 ^oC for 2 hours to get a carbon-free and high-crystalline surface. The laser used in the deposition was KrF (λ=248 nm) excimer laser with an energy density of 6 J/cm^2. Stoichiometric YBCO ceramics and STO single crystal were adopted for the target. During the deposition process the targets were rotated to reduce nonuniform erosion. The substrate was placed parallel to the target at a distance of 6 cm. During the deposition, the chamber was kept at 10^{-5} Pa. The deposited films were then annealed at 420 °C in an ambient of high oxygen pressure (up to 0.8 atm) for 1 hour before slowly cooled down to room temperature. High purity oxygen was used as reactive agent, which was introduced into the chamber through a needle valve. This helps ensure oxygen stoichiometry in the films.

3.2.2 Structural Characterizations

A number of techniques were employed to characterize the STO/YBCO multilayer. They include:

1) Reflective high-energy electron diffraction
2) X-ray diffractometer
3) Atomic force microscopy
4) Raman spectroscopy

3.2.2.1 Deposition Processing Monitored by RHEED

Indeed, the growth mode of the YBCO film on STO and LAO substrates were non-equilibrium process, and were sensitively on the balance various thermodynamic and kinetic factors related to the surface microstructure and phase formation, which can be controlled by adjusting deposition temperature, laser energy and pulse rate.

As mentioned above, at deposition temperature below about 1200°C, only three different growth modes can be achieved. Figure 3.2 shows the typical RHEED pattern and schematic diagram of these three growth modes. Among them, we are trying to get a 2D layer-by-layer growth which offers thin film with a smooth surface.

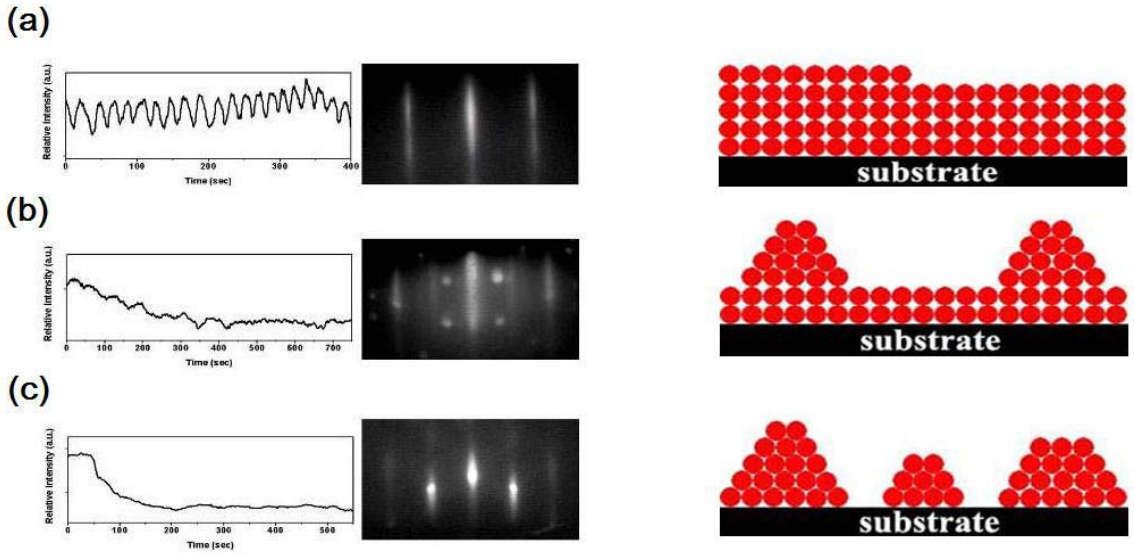

Fig. 3.2 Typical RHEED pattern and schematic diagram of these three growth modes: (a) 2D layer-by-layer, (b) SK growth, (c) 3D-island growth [Y. R. Li, 2004]

Figure 3.3 and Figure 3.4 show the RHEED pattern of YBCO grown on STO (001) with a polycrystalline growth and a 3D-island growth mode, respectively. Correspondingly the samples often exhibit poor crystalinity and the surface of the YBCO becomes rather rough. This would greatly debase the quality of ferroelectric thin films.

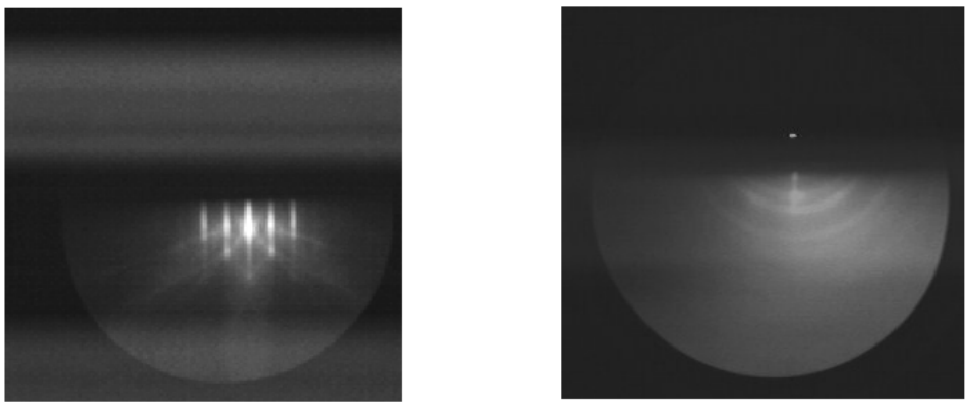

(a) (b)

Fig. 3.3 RHEED pattern of polycrystalline YBCO grown on STO substrates, (a) pattern of STO substrate, (b) YBCO thin film grown on STO substrate for 30 min

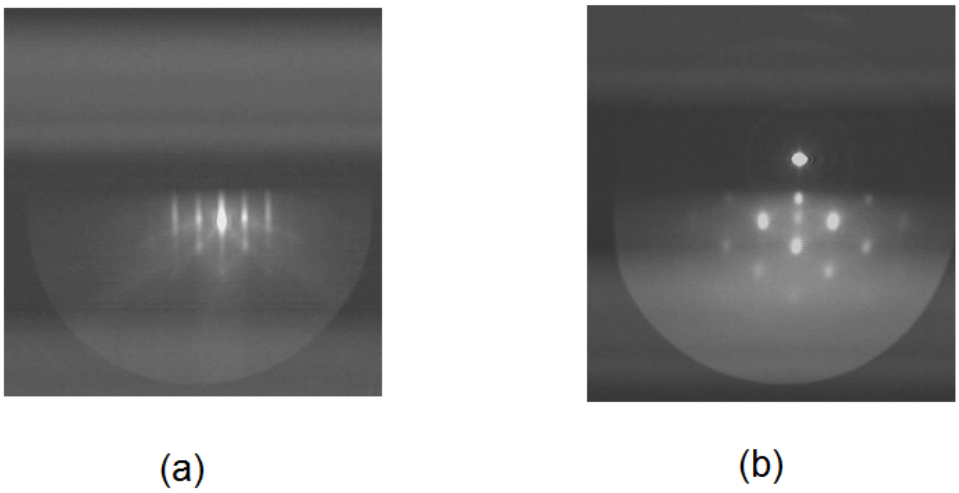

Fig. 3.4 RHEED pattern of YBCO grown on STO substrates with 3D-island growth mode, (a) pattern of STO substrate, (b) YBCO thin film grown on STO substrate for 30 min

The optimized processing conditions for YBCO thin films growth are summarized in table 3.1

Table 3.1 L-MBE deposition conditions for YBCO thin film.

Target	YBCO ceramic
Laser energy	160-180 mJ
Frequency	0.5 Hz
Pre-annealing temperature	750~800 °C
Substrate temperature	600~680 °C
Pressure	10^{-5} Pa
Deposition time	2 hours

3.2.2.2 STO/YBCO Multilayer Growth Mode

STO/YBCO/LAO samples prepared under the optimized conditions are found to have the following structural features: (1) relationship between STO/YBCO and YBCO/substrate both epitaxial alignment; (2) growth mode of YBCO on substrates and STO on YBCO are 2D-layer-by-layer growth. While other detailed structural information of a fabricated thin film is available only after a series of post-deposition structural characterization experiments, an *in-situ* observation of the RHEED of the sample surfaces gives useful information for accessing the quality of the film under preparation.

Fig. 3.5 shows an evolution of RHEED patterns of STO/YBCO films grown on LAO, as a function of time during the deposition. The information of growth mode could be obtained by *in situ* monitoring RHEED pattern and intensity. Fig. 3.5 (a) for LAO substrate annealed at the deposition temperature shows clear bright streaks, suggesting that the substrate surface has an atomically flatness. At the beginning of YBCO growth, the diffraction of substrate with bright streaky pattern fades away and changes into the spotty pattern as shown in Fig.3.5 (b). According to Braggs' law, it indicates that the YBCO starts to grow in 3D-island mode with a rough interface. The lattice constant of YBCO (*a*=0.3823 nm, b=0.3887 nm, c/3=0.3894 nm) is larger than that of LAO (0.379 nm), indicating that the YBCO films on LAO are under compressive strain. Such a compressive strain due to lattice misfit is associated with the change of

growth mode. With an increase of YBCO thickness, the intensity of the pattern becomes weaker and changes gradually back to a streaky pattern from 6 nm-thick YBCO. It suggests that the strain was gradually released. Beyond the thickness of 20 nm-thick YBCO film, the diffraction pattern shows clear streaks as seen in Fig 3.5 (c). It indicates that the YBCO is fully relaxed and remain a layer-by-layer growth mode. Further continuous growth of STO thin film was followed to deposit on YBCO/LAO. Fig. 3.5 (d) shows that a 2D layer-by-layer growth mode forms, which is clearly evidenced by the streaky pattern. As the lattice constant of STO (*a*=0.3905 nm) is quite similar to that of YBCO, the epitaxial STO films have been promoted on the former YBCO at the interface. Therefore, STO/YBCO/LAO multilayers are grown epitaxially with good quality.

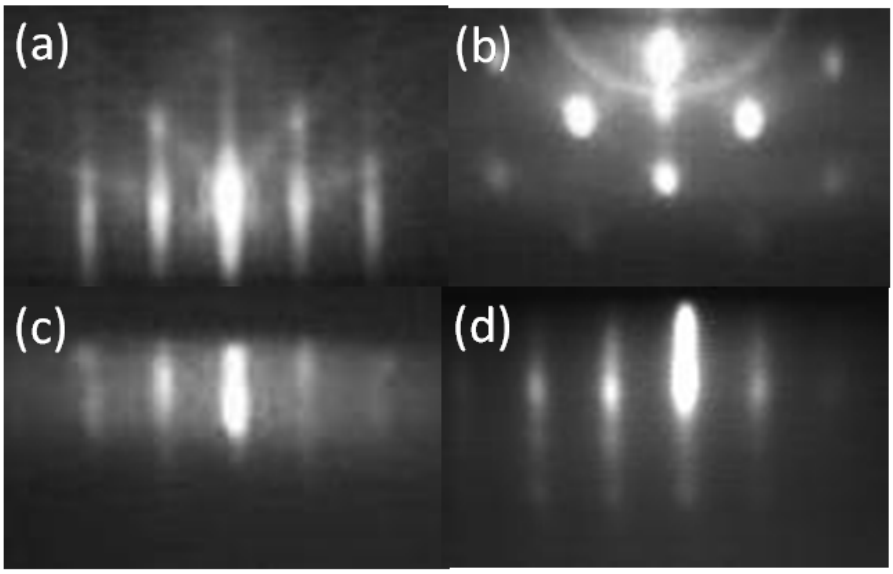

Fig. 3.5 The RHEED diffraction patterns (a) LAO substrate, (b) 6 nm YBCO thin film on LAO, (c) 20 nm YBCO thin film on LAO, (d) 300 nm STO thin film on YBCO/LAO substrate.

Figure 3.6 shows the RHEED patterns of STO/YBCO films grown on STO substrates, and has a similar revolution. Only the crystalinity of the thin film is not as good as grown of LAO substrates. It may be caused by the difference compressive strain and tensile strain.

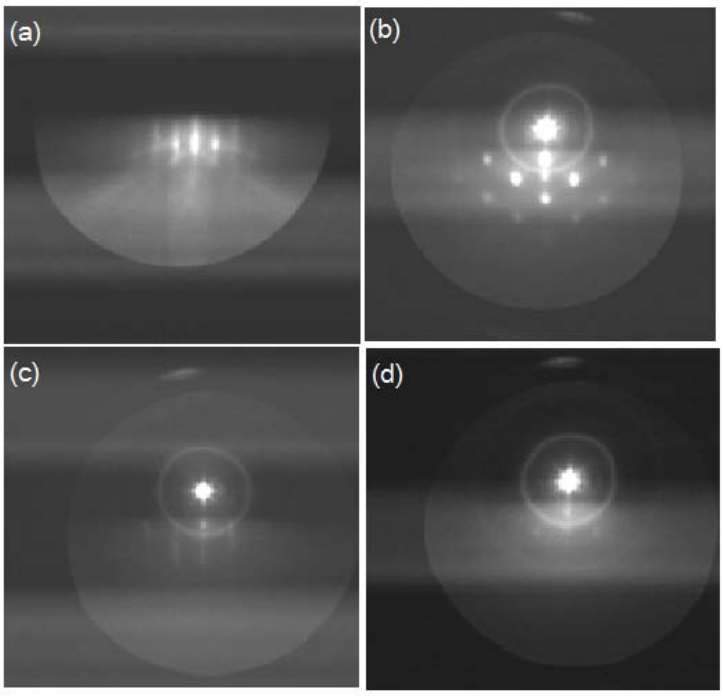

Fig. 3.6 The RHEED diffraction patterns (a) STO substrate, (b) 6 nm YBCO thin film on STO, (c) 20 nm YBCO thin film on STO, (d) 300 nm STO thin film on YBCO/STO substrate.

3.2.2.3 Crystallization Characterized by XRD

To confirm the epitaxial characteristic of STO/YBCO/LAO, we have measured XRD of the multilayer as shown in Figure 3.7. Only (00*l*) peaks of YBCO and (00*l*) peaks of STO can be observed, indicating that the *c* axis of both layer are perpendicular to the substrate surface. Calculations obtained from the parameters of XRD shown in Figure 3.7 yield a lattice constant of 0.390 nm for the STO film. Thus, the deposited STO film has a lattice parameter very close to the bulk material. It reflects that the relaxation of strain of 300 nm-thick STO film has largely completed. Typical full width at half maximum (FWHM) values of the rocking curves from the STO (002) diffraction peak was 0.62 ^{o}. It implies that the films have good quality along (00*l*) orientation.

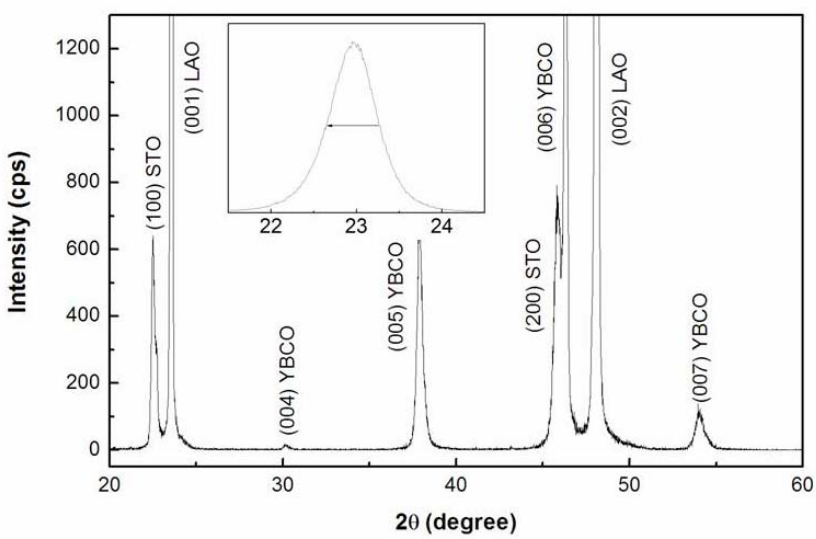

Fig. 3.7 XRD θ-2θ scan of STO/YBCO/STO. The inset indicates the rocking curve for STO (002).

3.2.2.4 AFM Morphology of YBCO

In order to understand the surface structure of the YBCO films in whole growth process, AFM was employed to study the surface morphology. Figure 3.8 (a) is an AFM image of YBCO films grown at 160 second, the root mean square roughness value of the surface is 4.28 nm, the surface morphology appears to consist of grains with various shapes, which is mainly attributed to the island growth mode and the in-plane tensile strain since both *a* and *b* axes are stressed by the large lattice mismatch between the films and substrates. Figure 3.8 (b) is an AFM image of YBCO films grown at 1200 second. With the thickness increased, the as-grown film has very smooth surface morphology which is possibly associated with the 2D-layer-by-layer growth mode with strain relaxed.

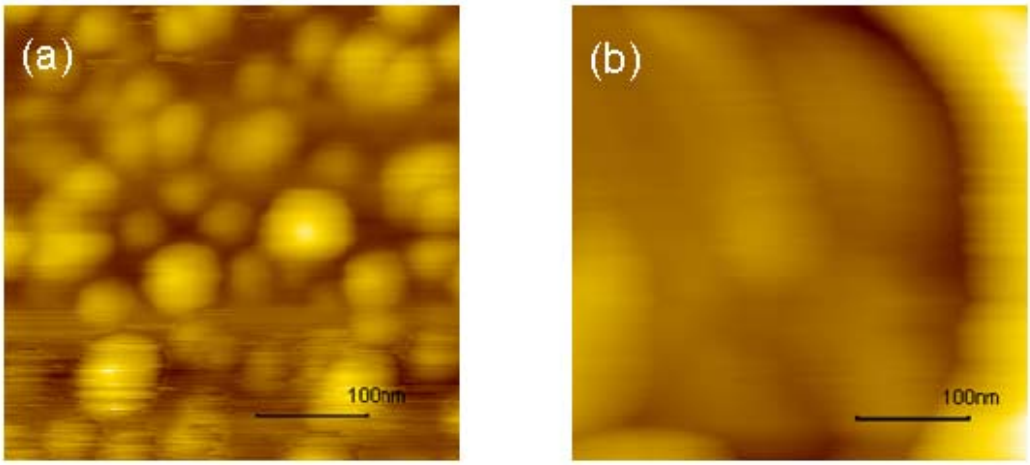

Fig. 3.8 AFM images of the surface of YBCO on STO substrates. (a) 160s, (b) 1200s

Based on the above-mentioned experimental data, the systematical kinetics process about the growth of YBCO/STO films under the tensile stress was suggested. In the case of YBCO/STO, YBCO film grows coherently epitaxially on the STO substrates. The tensile stress at this stage was not readily relaxed due to the extremely small film thickness at initial stage. The YBCO film was tensile in-plane due to the small difference of lattice parameter between film and substrate. With further growth, the stress could be relaxed by the formation of misfit dislocations as well as defects in the film to achieve the equilibrium state of energy, as shown in (Figure 3.8 (a)). After the formation of misfit dislocation and defects, the distributions of stress at the interface were nonuniform. The areas where misfit dislocation located underneath were stressed, where those regions between neighboring misfit dislocations came into being the centers of nuclear. Adatoms on the film surface will form three dimension islands within the areas of nuclear centre through a surface diffusion process. However, with further growth, the tensile stress release gradually. Due to the extremely low deposition and high temperature, particles deposited on the surface were offered sufficient atomistic surface mobility, which, especially, satisfied the thermodynamic and kinetic requirement for structural stability under two dimension growth fashion. Then a very smooth surface morphology was achieved, which evidently were confirmed by (Figure 3.8 (b)).

3.2.2.5 Lattice Dynamics Study

It is well known that the lattice dynamics is of central significance in the understanding of physical properties of STO. We attempt to study the lattice dynamics of STO thin films using Raman scattering. However, single layer of STO is transparent to excitation light in Raman measurement. It is difficult to obtain and analyze Raman signal from a sample of single STO layer. Fortunately, YBCO layer in our STO/YBCO/LAO multilayers can be used as a reflective layer so that the signal from the transparent STO films will not be overwhelmed by the substrate signals [I. A. Akimov, 2000]. The Raman signal from the STO films can be observed with the technique. Figure 3.9 shows the Raman spectra of STO/YBCO/LAO multilayers measured from 20 to 300 K. In principle, STO single crystal has a centrosymmetric structure, cubic at high temperatures and tetragonal below 105 K. The zone-center optical phonons are of odd parity, and consequently are not Raman active. The Raman spectra of STO films in Figure 3.9 exhibit dramatic difference compared with that of STO single-crystal [D. A. Tenne, 2004]. According to the hyper-Raman scattering result for single crystals, STO has optical phonons at 88(TO_1), 175(LO_1, TO_2), 474(LO_3), 545(TO_4), and 795(LO_4) cm^{-1} [V. N. Denisov, 1987; H. Vogt, 1981], where TO stands for transverse optical and LO for longitudinal optical branches. In addition to the peaks related to YBCO layer, two peaks at 480 and 541 cm^{-1} in Figure 3.9 may be associated with the scattering by the 474 cm^{-1} (LO_4) and 545 cm^{-1} (TO_4) STO bulk phonons, respectively. Both of them are symmetry forbidden in the Raman spectra for the single crystal. In the connection with Figure 3.5(d), although the RHEED pattern of STO film demonstrates that the growth switches to good crystalline growth with highly orientation in 2D layer-by-layer growth, the streaky RHEED pattern of the as-grown STO films still

looks dim compared with the bright streaky patterns from STO single crystal. It could be speculated that the STO thin films consisted of many defects and nanoscale second phase. For STO thin films, interfacial effect and oxygen vacancies may contribute to the lowering of symmetry and the breaking of the central symmetry as shown in Figure 3.9. Furthermore, the intensity of LO_4 and TO_4 phonon decreases as the temperature increases. This result is consistence with previously reported results on titanate thin films [S. Gupta, 2001; D. A.Tenne, 2004].

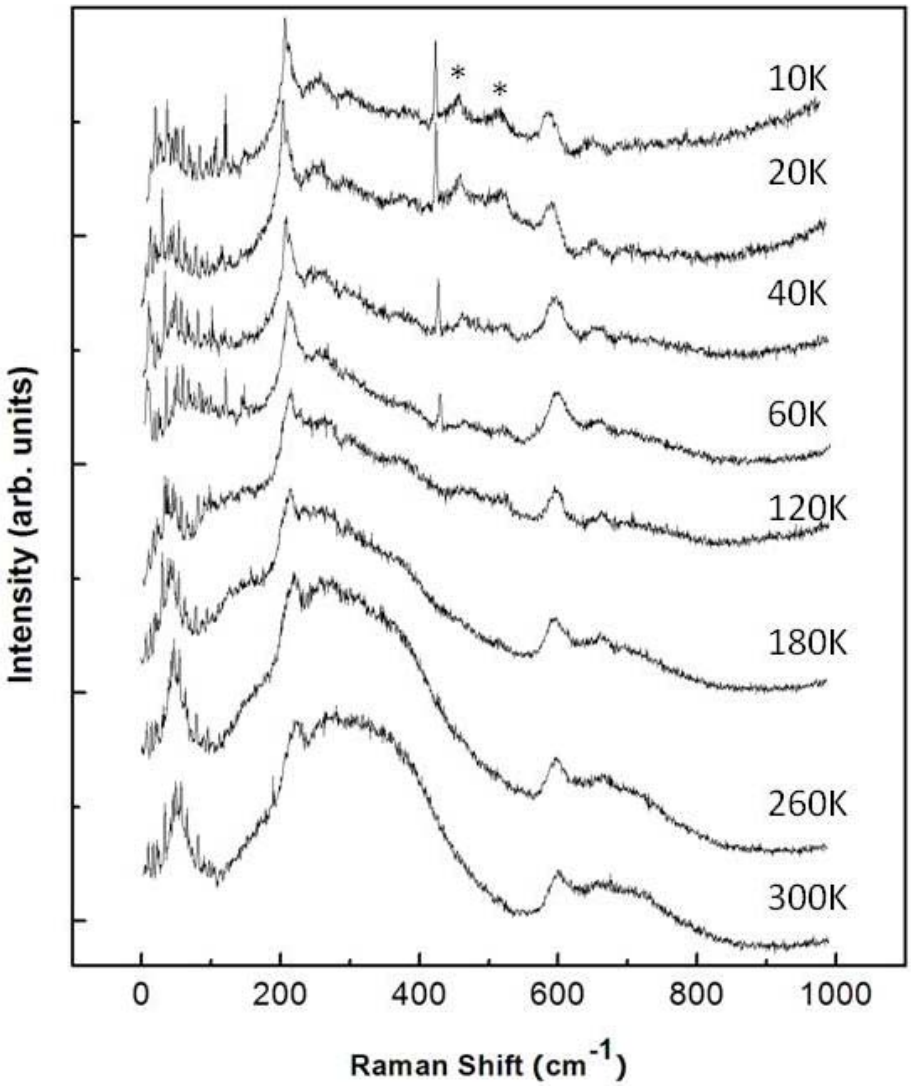

Fig. 3.9 Temperature evolution of Raman spectra for STO/YBCO thin film on LAO substrates, the stars shows positions of TO_4 and LO_4.

3.3 Electrical Characterization of STO/YBCO/LAO

The dielectric constant and loss for STO/YBCO/LAO was measured within a temperature range between 80 K and 273 K as shown in Figure 3.10. At room temperature, the dielectric constant ε of STO films was about 280. And the ε value increase as the temperature decreases. The dielectric loss tangent of STO thin film varies within a wide range of temperatures, and the lowest loss tanδ is about 0.012 at T~170 K. The dielectric properties exhibit strongly dependant on the temperature. In addition, the dielectric constant at different measured frequencies is roughly same for all temperatures. On the other hand, Figure 3.10 indicates that the loss tangent of STO films is much higher when the frequency applied is 10 kHz. At any rate, the dielectric properties of STO thin films are not as good as those of single crystal. As expected, the dielectric constant at 80 K is only 550, one to two orders of magnitude lower than that of the STO single crystal. The dielectric loss is one to two orders of magnitude higher than that of the STO single crystal. Although the use of intermediate layer YBCO in the work may reduce the strain and interfacial effects, the formation of dislocations at the interface between STO and YBCO serves to relieve the strain as shown in Figure 3.5. In STO thin films with those defects, one-phonon absorption and phonon scattering on localized phonons near defects may give rise to extra losses.

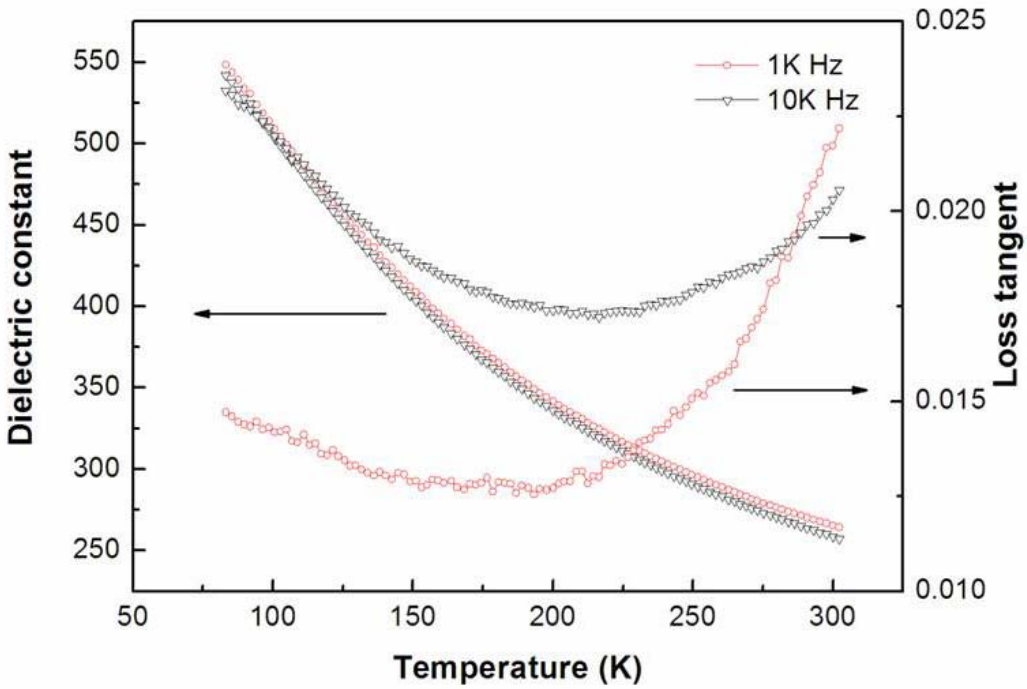

Fig. 3.10 Temperature dependence of the dielectric constant and loss measured at 1 kHz and 10 kHz for STO/YBCO/LAO.

3.4 Summary

In this chapter, we have demonstrated LMBE technique to control the growth process of YBCO and STO perovskite thin films. Well-ordered heterostructure of STO/YBCO/LAO and STO/YBCO/STO multilayers was achieved. An evolution of growth mode during the growth of thin films was observed. As a result, the formation of dislocations at the interface between STO and YBCO may serve to relieve the lattice mismatch induced strain. The Raman spectra of STO films exhibits dramatic difference

compared with that of STO single-crystal. Both measured temperature and frequency can affect the dielectric properties of STO/YBCO/LAO heterostructure. Our results indicate that strain and defects may contribute to the lowering of symmetry in STO films, and therefore change dielectric properties of STO thin films.

CHAPTER 4

GROWTH AND PROPERTY CHARACTERIZATION OF $SrTiO_3$/GaAs AND $BaTiO_3$/$SrTiO_3$/GaAs

4.1 Introduction

Integration of functional oxide thin films with semiconductors has attracted considerable attention in recent years [M. Hong, 1999; R. A. McKee, 2003]. The primary motivation has been the development of a gate dielectric for downscaling of MOSFETs technology, which makes a transition from traditional poly-Si/SiO_2/Si to a more complex metal/high-K/semiconductor system [G. D. Wilk, 2000]. Also, hetero-epitaxy of crystalline oxides on semiconductor provides new opportunities for integration of various functional oxides or carbon nanotube transistors [B. M. Kim, 2004; S. Migita, 2001; A. K. Pradhan, 2005]. It has been a long-sought goal for successful growth of epitaxial oxides on Semiconductor. Because of the structural registration between oxide and semiconductor in an epitaxial structure, crystalline oxides on semiconductor could potentially provide an interface with lower defect density and better electronic properties [C. J. Först, 2004; R. A. McKee, 2003].

GaAs with a zincblende structure (a= 5.65 Å) is the new generation III-V semiconductor. Compared to Si, GaAs has a higher saturated electron velocity and higher electron mobility, allowing transistors made from it have the potential for enabling future high-speed applications at very low power-supply voltages [R. Chau, 2005]. Figure 4.1 shows the electron velocity versus electric field curves for pure GaAs and Si. Also, GaAs has a direct band gap. Crystalline perovskite titanate thin films on GaAs are fundamental to a wide range of systems, spanning high-speed devices, optoelectronic sensors and spintronics. For example, great efforts have been made to develop GaAs-based metalferroelectric-insulator-semiconductor (MFIS) functional heterostructure [M. Hong, 1999; M. Passlack, 2002; K. D. Choquette, 1997]. Figure 4.2 shows the two different coplanar microwave device design.

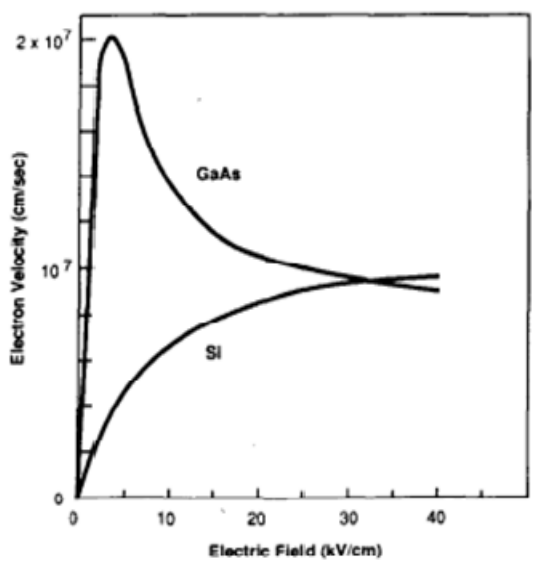

Fig. 4.1 Electron velocity versus electric field curves for pure GaAs and Si [D. E. Fulkerson, 1992]

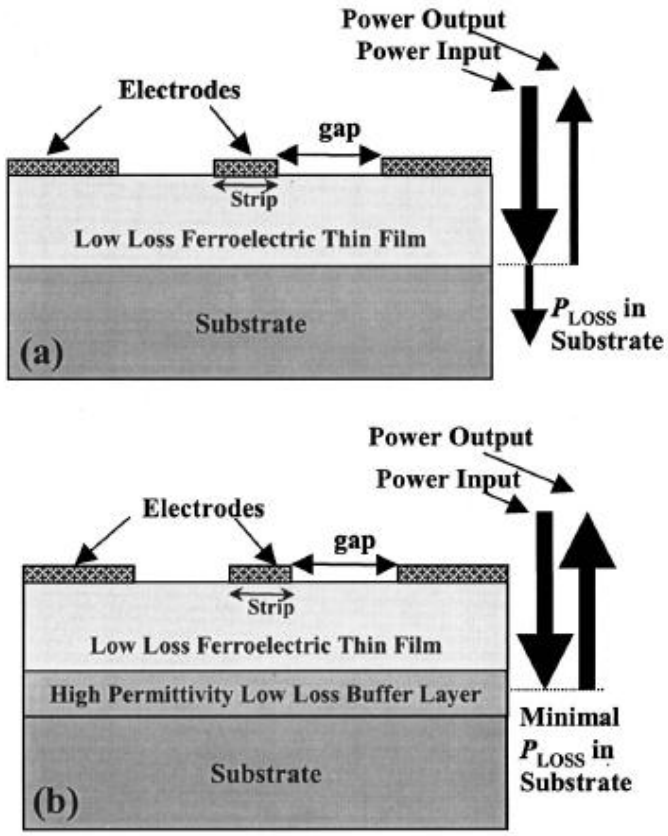

Fig. 4.2 Coplanar device design showing (a) tunable low-loss thin film deposited on lossy substrate and (b) the tunable low loss thin film integrated with the same lossy substrate utilizing a high permittivity, low-loss buffer layer to mitigate the power loss in the substrate [M. W. Cole, 2002]

Much research has been focused on the electrical properties of amorphous and polycrystalline MFIS structure via a buffered insulator layer [M. Hong, 2000; T. E. Murphy, 2004; D. Chen, 2004]. The union of perovskite titanates and semiconductors

presents potentially the significant challenge to the basic study of growth. The epitaxial growth of perovskite titanate thin films on Si has been studied extensively in the last decades [R. A. Mckee, 1998; H. Li, 2003; J. H. Hao, 2005; J. L. Li, 2007], while integration with GaAs has attracted much less attentions. Murphy *et al.* reported the ferroelectric properties in epitaxial grown BTO on GaAs via MgO buffer and found that these properties are greatly sensitive to the interface structure and buffer thickness [T. E. Murphy, 2004]. Chen *et al.* reported that optical waveguiding was observed in BTO/MgO/Al_xO_y/GaAs structure showing primary optical confinement in the BTO thin film [D. Chen, 2004]. It is recognized that interface structure and crystal orientation have played an important role in controlling the ferroelectricity and other electrical properties. Therefore, synthesizing highly single crystalline MFIS heterostructure via an epitaxial buffer layer and establishing a comprehensive understanding on the synthesis-interface-property relationship become critical issues. Recent study showed that the MgO with a thickness of few nanometers on GaAs may suffer from the high charge injection while increasing reverse bias voltage due to a MgO/GaAs interface current effect [J. C. Le Breton, 2007]. Ferroelectric oxides on MgO buffered GaAs always exhibits weak ferroelectric properties with a large leakage [T. E. Murphy, 2004]. Therefore, the development of GaAs-based ferroelectric devices is hindered by the poor properties of perovskite titanates/GaAs heterostructures.

Compared with MgO, $SrTiO_3$ (STO) is an incipient ferroelectric material with a large variable dielectric constant and low loss, has been intensely studied for applications in tunable microwave devices [X. X. Xi, 2000; W. Chang, 2005]. STO also

possesses a cubic perovskite structure and has a lattice (a= 3.905 Å) closely matched with a large number of functional perovskite materials. Thus, STO has widely been used as a suitable interface template for growth of high quality functional ferroelectric, ferromagnetic and multiferroelectric oxide [A. Lin, 2001; A. Talin, 2002; S. Y. Yang, 2007; J. Wang, 2005; Y. Mukunoki, 2005; Y. Wang, 2005]. Meanwhile, the epitaxial growth of STO on Si has been studied extensively. Those STO films grown directly on Si using various deposition techniques were usually polycrystalline with randomly oriented grains at the beginning [F. Sánchez, 1992; F. Sánchez, 1998; O. Nakagawara, 1995; J. Q. He, 2002; Z. Wamg, 2001]. The pioneering work of McKee et al. deposit the epitaxial STO on Si (001) with a $SrSi_2$ submonolayer interface by molecular beam epitaxy (MBE) technique [R. A. Mckee, 1998; R. A. Mckee, 2001]. Other groups also have been carried out on the growth of STO (001) on Si (001) with various single buffer layers or multi-buffer layers [S. Migita, 2001; T. Yamada, 2003; Y. Z. Yoo, 2003]. After optimize the details of deposition conditions and specific growth sequences, epitaxial STO (110) films on Si without any buffer layer by pulsed laser deposition (PLD) technique was achieved [J. H. Hao, 2005]. In order to get low interface defect and better electronic property, high quality single-crystal film is required. Unfortunately, the successful epitaxial growth of STO thin film on GaAs is difficult due to structural incompatibility and interdiffusion between GaAs and STO. So far, the epitaxial thin film of STO grown on GaAs has only been achieved via a complex molecular beam epitaxy (MBE) with a submonolayer of titanium as buffer [Y. Liang, 2004].However, The O vacancy STO exhibited n-type semi conductivity and was limited for further electrical properties investigation.

In this chapter, we report our work on the integration of STO thin films on GaAs by means of the laser molecular beam epitaxy first, Studies of the microstructure and dielectric properties of these STO/GaAs hetero-epitaxial structures are also presented. Base on STO buffered GaAs, epitaxial BTO thin film was then deposited, Enhanced ferroelectric properties and transport characteristics of the perovskite titanates/GaAs heterostructure are demonstrated.

4.2 Structural and Dielectric Properties of STO/GaAs

4. 2.1 STO Thin Film deposition by Laser-MBE

Thin films of STO were deposited directly on GaAs (001) substrates by LMBE. As the surface oxides can desorb at about 600 °C, the GaAs wafer, was first *in situ* heated up to 650 °C in vacuum for 2 min to remove the native oxide layer. A single-crystalline STO target was ablated using a KrF excimer laser of 248nm wavelength with an energy density of 6J/cm^2. The target was rotated during the deposition process to reduce nonuniform ablation. The substrate was placed parallel to the target at a distance of 6 cm. The growth rate of STO was about 0.03 nm /pulse. During the deposition, the chamber was evacuated to a base pressure of 5×10^{-5} Pa to avoid oxidation of the GaAs substrate; the substrate temperature was kept at about 600 °C. The deposited films were then *in situ* annealed at 420°C in ambient of high oxygen pressure for a few hours before cooled down to room temperature. This was to ensure oxygen stoichiometry in the STO

films. The optimized processing conditions for STO thin films growth are summarized in table 4.1. A reflective high energy electron diffraction (RHEED) system with an incident energy of 30 kV and an incident angle of about 2.5° was used to monitor the film growth process. In order to study the dielectric properties of the STO/GaAs heterojunction, Pt spot electrodes with a diameter of about 0.2 mm were fabricated on the top. P-type GaAs substrate (resistivity is 6 Ω cm) was used as the bottom electrode. Electrical properties of the STO films were investigated using a Hewlett Packard 4294A LCR meter.

Table 4.1 L-MBE deposition conditions for STO thin film on GaAs.

Target	STO single crystal
Laser energy	6 J/cm^2
Frequency	1 Hz
Pre-annealing temperature	650 °C
Pre-annealing time	2 min
Target distance	6 cm
Pressure	5×10^{-5} Pa
Growth rate	0.03 nm/pulse
Substrate temperature	600 °C
annealing temperature	420 °C
annealing time	1~2 hours

4.2.2 RHEED Monitoring of STO/GaAs Growth

Figure 4.3 is the RHEED patterns showing the epitaxial features of the STO film grown on GaAs substrate. In comparison with GaAs zincblende structure crystal, the STO has a perovskite cubic structure at room temperature. Both GaAs (face-centered cubic a = 0.56 nm) and STO (primitive cubic a＝0.3905 nm) exhibit a cubic symmetry. Thus, the lattice mismatch between STO and GaAs is relatively large at about 31%. However, according to RHEED patterns in Figure 4.3, good epitaxial nature of STO film on single crystal p-GaAs substrate could be observed. At the initial growth stage of GaAs film, the laser repetition was programmed to 1 Hz. The diffraction spots of GaAs representing (200) plane cluster in the RHEED pattern (Fig. 4.3(a)) gradually disappeared (Fig. 4.3(b) and Fig. 4.3(c)). Then two elongated bright spots emerged with a wider separation (seen in Fig. 4.3(d)). According to the Bragg's diffraction law, epitaxial STO film starts to grow with an in-plane rotation. The spotty diffraction pattern in Fig. 4.3(e) indicates that the interface at the first few atomic layers is not quite smooth. At subsequent growth the film thickness was increased. Conspicuous streaky diffraction patterns of the (001) plane of STO could be observed (Fig. 4.3(f)). This suggests that the growth becomes a two dimensional layer-by-layer mode as the STO film thickens. During the whole growth process, no unidentifiable RHEED patterns were detected. Apparently no other unstable phases existed despite the complex stoichiometry of titanium oxide. We have performed comparative studies on the crystallinity of STO thin films with different deposition pressure, substrate temperature and laser repetition rate. It seems that the quality of the STO thin films depends on the growth condition

such as oxygen pressure, deposition rate, and deposition temperature, *etc*. For example, the deposition temperature was found to be critical in obtaining single (100)-oriented STO thin films. Deposition at below 550°C resulted in amorphous film; no RHEED and XRD pattern were observed. Growth at temperature above 690°C, however, layer-by-layer sublimation from GaAs was found [M. Ishida, 1978].

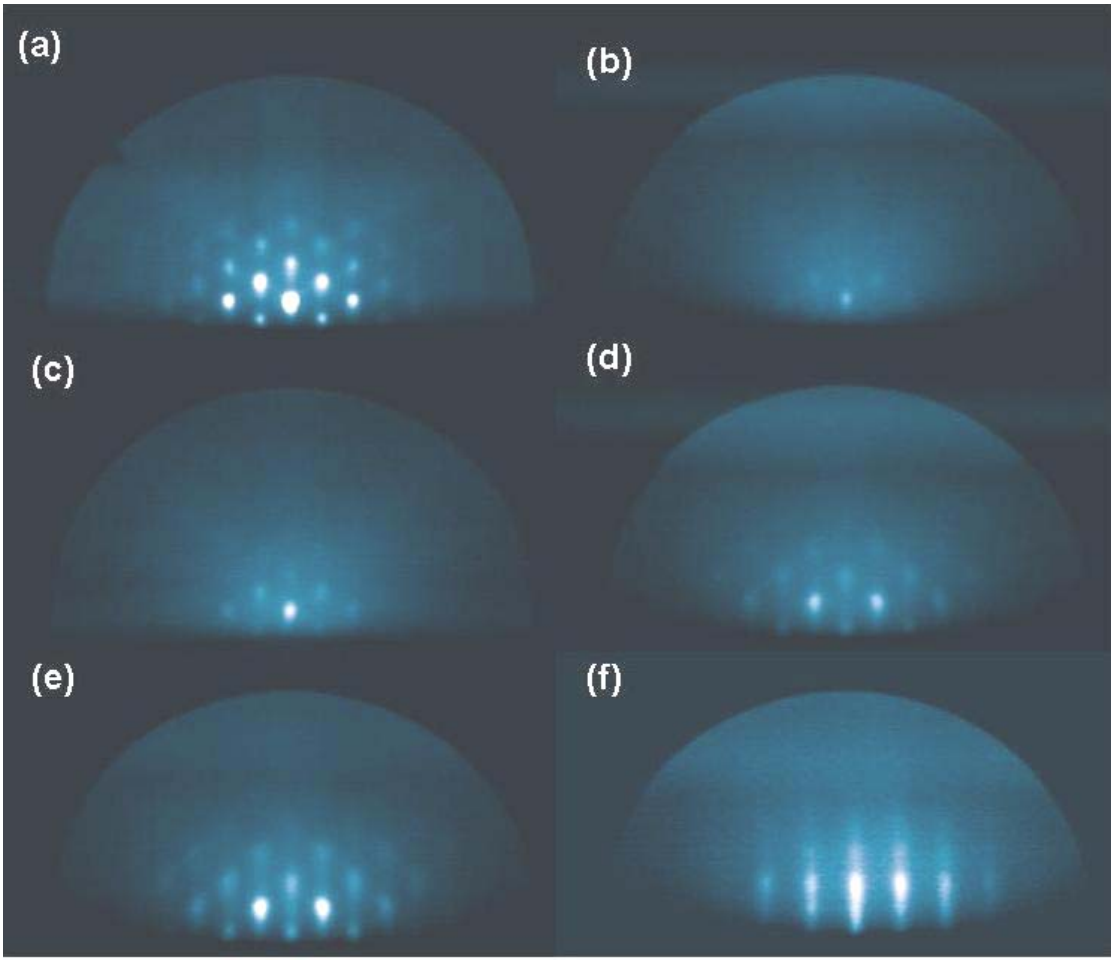

Fig. 4.3 The RHEED diffraction patterns recorded as a function of film thickness during the process of STO growth, (a) 0, (b) 0.5 nm, (c) 1 nm, (d) 2 nm, (e) 3 nm, (f) 300 nm.

4.2.3 Crystallization Characterized by XRD

X-ray diffraction (XRD) was employed to examine the in-plane and out-of-plane relationships between the STO thin film and GaAs substrate. Fig. 4.4(a) displays a typical x-ray θ-2θ diffraction pattern of a 3000Å thick STO layer on GaAs. Only diffraction peaks of STO (001) and (002) were observed. This suggests that the as-grown films are a single (001) phase oriented. Both STO and GaAs have cubic unit cells, and the lattice constant is a_{STO}=0.3905 nm and a_{GaAs}=0.565 nm, respectively. For STO (001) parallel to the (001) of GaAs, the lattice mismatch is $\left(\left|\alpha_{STO}-\alpha_{GaAs}\right|/\alpha_{GaAs}\right)\times 100\% = 31\%$. This value is considerably large for a good epitaxial film growth. However, the mismatch would be relatively small for a 45° in-plane rotation of STO respect to GaAs, i.e. $\left(\left|\sqrt{2}\alpha_{STO}-\alpha_{GaAs}\right|/\alpha_{GaAs}\right)\times 100\% = 2.2\%$. The XRD 360°-φ scan results confirm the hetero-epitaxial relationship between STO and GaAs. The 45° in-plane rotation between STO and GaAs is evident, as seen in Fig. 4.4(b). The relationship between the STO lattice and GaAs lattice is schematically shown in Figure 4.5. The interface strain induced by lattice mismatch is gradually relaxed as the film thickness increases. Calculations based on parameter obtained the XRD shown in Fig. 4.4(a) yield lattice constants of 0.390 nm and 0.565 nm for the STO film and the GaAs substrate respectively. Thus the STO film has a lattice parameter very close to the bulk material. Although the measurement is for out-of-plane lattice only, it nevertheless reflects that the strain of the STO film has relaxed at the film thickness.

Rocking curve measurement of the STO film in the inset of Fig. 4.4(a) showed a full-width-at-half-maximum (FWHM) value of 1.6°. This somewhat large FWHM value is the result of the degraded crystallinity of the STO thin films grown on lattice mismatched (100)-oriented GaAs substrates via a 45° in-plane rotation.

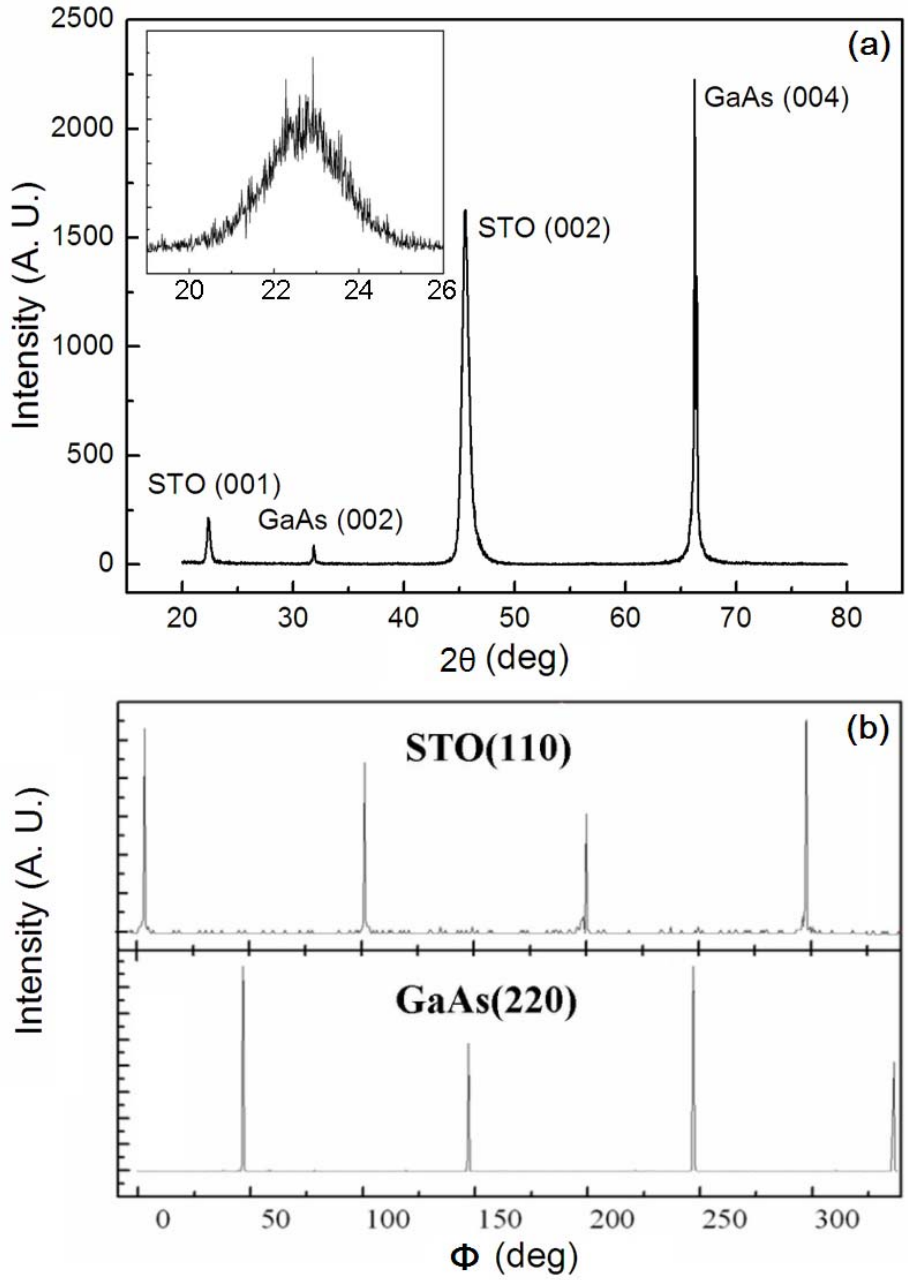

Fig. 4.4 XRD of STO/GaAs heterostructure. (a)θ-2θ scan. The inset indicates the rocking curve for STO; (b)Φ scan.

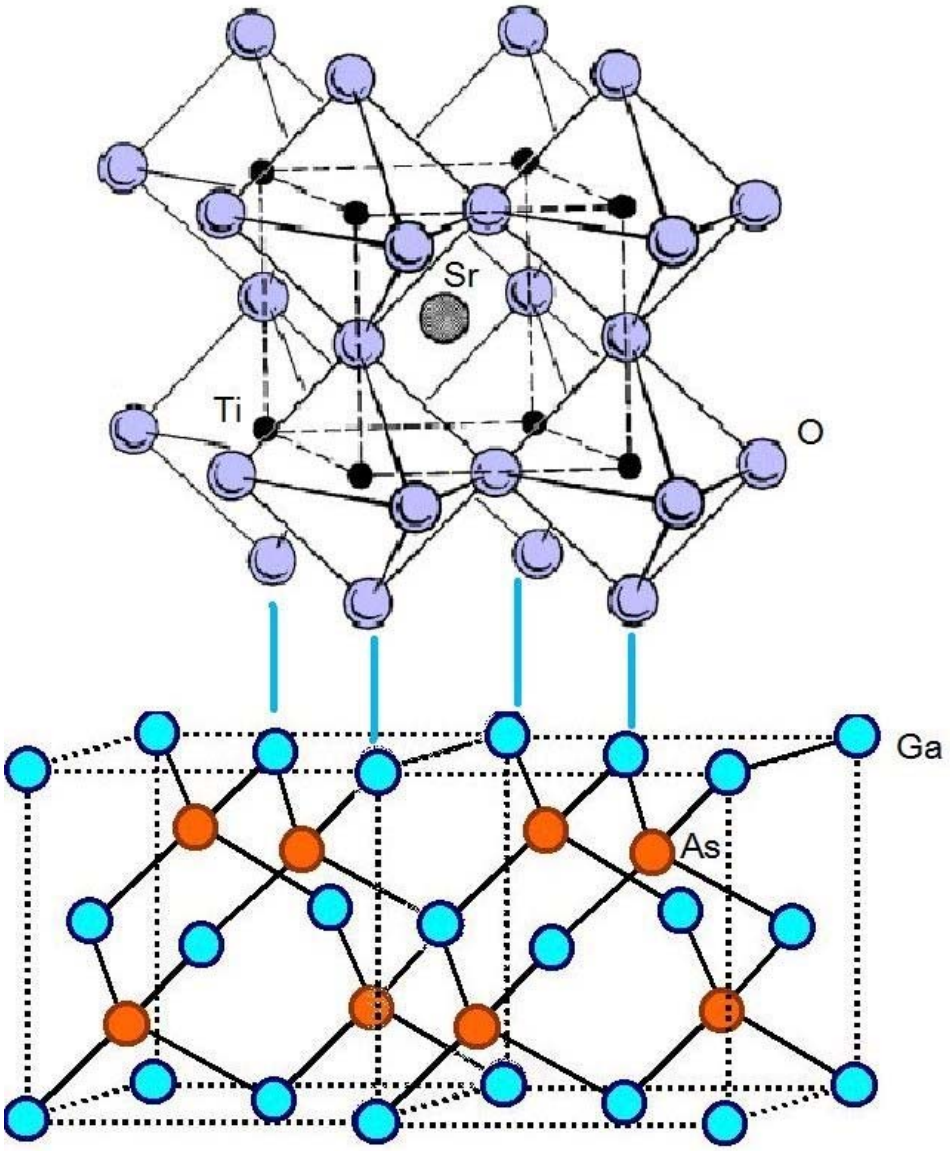

Fig. 4.5 Epitaxial relationship of STO lattice and GaAs lattice. There is a slight distortion in the STO lattice as compared with bulk material. There is a 45° rotation between the (001) direction of GaAs and (001) direction of STO.

4.2.4 Surface Morphology of STO/GaAs

As a potential template for integration functional perovskite oxide with GaAs, the surface morphology of the STO layer is of a major concern. We use atomic force microscopy (AFM) to study the surface of the STO/GaAs heterostructure. Fig. 4.6 shows a 2×2 μm^2 area surface morphology of the cubic $SrTiO_3$ films grown on GaAs. The as-grown film has very smooth surface with a root-mean square (RMS) roughness values of 0.84 nm. Such good surface smoothness is attributed to the result of layer-by-layer growth mode shown in Fig.4.3.

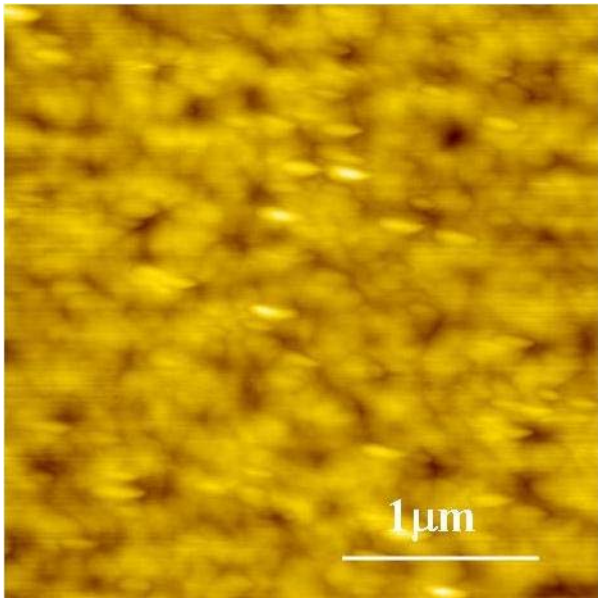

Figure 4.6 AFM images of the surface of 300 nm STO thin films grown on GaAs substrate.

4.2.5 Interfacial Structure of STO/GaAs

Transmission electron microscopy (TEM) studies were carried out on a JEOL JEM-2011 microscope operated at 200 kV. The cross-sectional image in Figure 4.7 shows that the STO film was crystallized and about 150 nm thick. The density of dislocations is very high near the interface and is reduced as the film grown thicker. Selected area diffraction patterns (SAD) taken at A1, A2, A3 are demonstrated in Figure 4.8. The highly ordered electron diffraction spots of STO lattice also confirmed that the STO film is highly epitaxially grown on the (001) surface of GaAs.

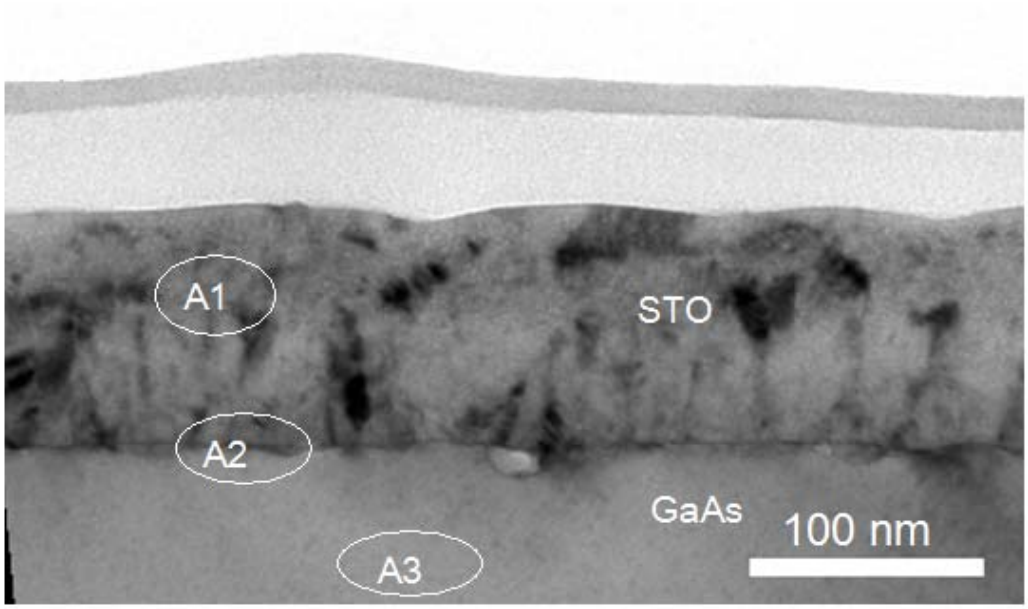

Fig. 4.7 The cross-sectional transmission electron microscope image of STO/GaAs.

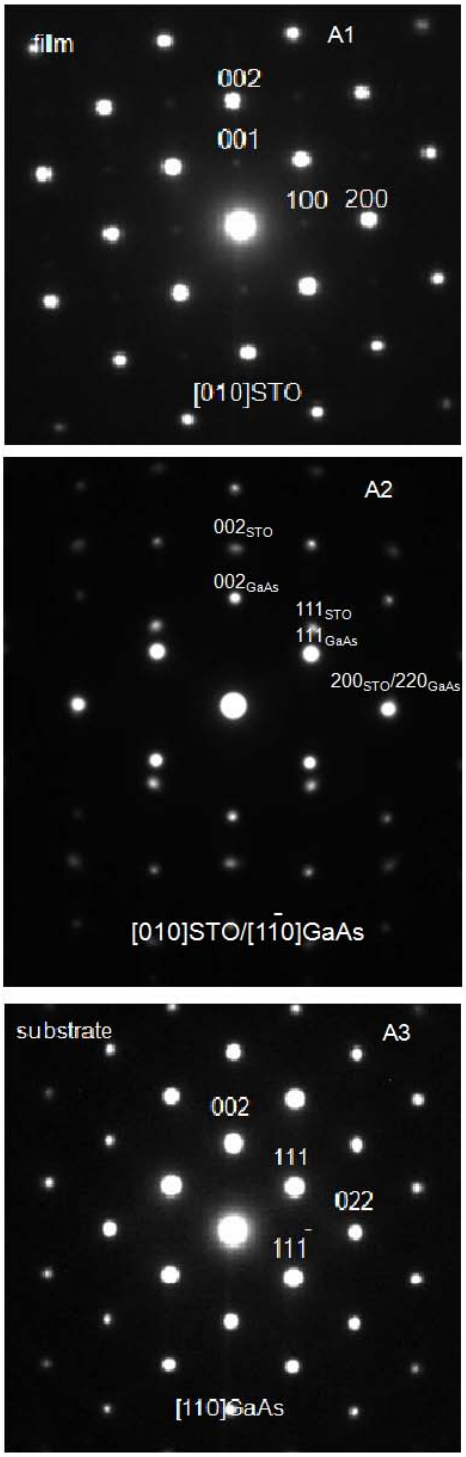

Fig. 4.8 Selected area diffraction patterns of STO/GaAs taken at A1, A2, A3.

4.2.6 Electrical Characterization of STO/GaAs

Fig. 4.9 shows the variation of dielectric properties of the STO film as a function of frequency at room temperature. The bulk dielectric constant of STO was approximate 300. As shown in Fig. 4.9, the experimental dielectric constant value of STO film was smaller compared to that of STO bulk and decreased significantly at increased frequency. The dielectric loss of the film was less than 0.02 for all values of measured frequency. According to the Fig. 4.3(b) and (c), an in-plane rotation of STO is occurred. This reduced dielectric constant at room temperature may be attributed to the effect of GaAs as the bottom electrode and/or charge dissipation at the disordered STO/GaAs interface. Similar result was found in other researchers' work [Y. Z. Yoo, 2003].

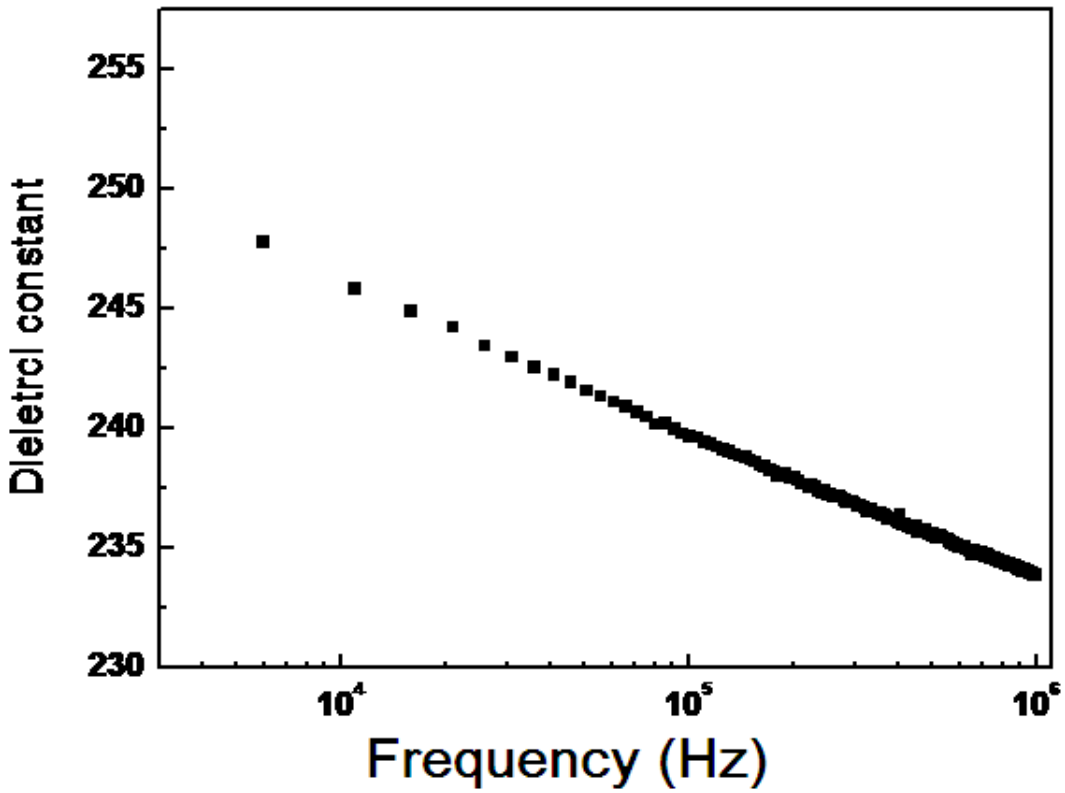

Fig. 4.9 Dielectric constant of 300 nm STO film as a function of frequency at room temperature.

4.3 Interface Structure and Electric Properties of BTO/STO/GaAs

4. 3.1 Processing Technique

The BTO/STO/ GaAs (001) heterostructure was grown by O_2 flowing pulsed laser molecular beam epitaxy system with an operation wavelength of KrF (λ＝248 nm). The laser energy density was about 6 J/cm^2 at a frequency of 1 Hz. A system of

reflective high energy electron diffraction (RHEED) was used to monitor the film growth process. As our recent report, STO layer was firstly deposited on GaAs (001) substrates at 600 °C [Z. P. Wu, 2008]. Then, the buffered GaAs was heated to 650°C and the subsequent ferroelectric BTO film with was grown under a flowing O_2 atmosphere of 1 Pa. The deposited films were then *in situ* annealed in ambient of high oxygen pressure before cooled down to room temperature. The deposition parameter of STO and BTO are summarized in table 4.2 and table 4.3. Finally, Pt electrodes were deposited for electrical measurements. P-type GaAs was used as a bottom electrode in our measurement. The resistivity of used GaAs wafer was estimated to be 6 Ω·cm. The film structure was determined by X-ray diffraction (XRD), and the interface characteristic was investigated by transmission electron microscopy (TEM). The dependence of current density on electrical field (*J*-*E*) of the system was measured. The ferroelectric properties were measured by using a ferroelectric test system (Radiant Inc).

Table 4.2 L-MBE deposition conditions for STO buffer layer on GaAs.

Target	STO single crystal
Laser energy	6 J/cm^2
Frequency	1 Hz
Pre-annealing temperature	650 °C
Pre-annealing time	2 min
Target distance	6 cm
Pressure	5×10^{-5} Pa
Growth rate	0.03 nm/pulse
Substrate temperature	600 °C

Table 4.3 L-MBE deposition conditions for BTO thin film on STO buffered GaAs.

Target	BTO ceramic
Laser energy	6 J/cm^2
Frequency	1 Hz
Target distance	6 cm
Pressure	O_2 : 1 Pa
Substrate temperature	650 °C
annealing temperature	420 °C
annealing time	1~2 hours

4.3.2 RHEED Monitoring of BTO/STO/GaAs growth

The RHEED patterns (Fig. 4.10) show the epitaxial features of BTO films grown on GaAs substrates using STO as a buffer layer. The diffraction spots of GaAs representing (002) plane cluster in the Fig. 4.10(a) gradually faded away as the STO started to grow. Fig. 4.10(b) shows the diffraction pattern with two unit cell of STO (about 8 Å), indicating the film was coherent at the onset of the STO growth. Then two elongated bright spots emerged with a wider separation could be observed. According to the Bragg's diffraction law, STO unit began to grow with a 45° in-plane rotation on GaAs to get a comfortable lattice match due to a large mismatch between STO (a= 3.905 Å) and GaAs (a=5.65 Å), which is consistent with the observation in ref [Y. Liang, 2004]. The spotty diffraction pattern in Fig. 4.10(b) also suggests STO possibly grew in coherent two-dimensional-island behavior at the STO/GaAs interface, which may be due to the large number of dislocation due to mismatch strain between STO and GaAs. This coherent behavior remained with film thickness up to approximately 30 Å as shown in Fig. 4.10(c), then the spot gradually faded away when thickness was greater than 30 Å, suggesting that the STO film began to relax when the growth went beyond this thickness. For the subsequent growth of BTO film on STO buffered GaAs, conspicuous streaky diffraction patterns of the (001) plane of BTO could be observed in Fig. 4.10(d). This unchanged streaky diffraction pattern indicates that the growth of BTO becomes a two dimensional layer-bylayer growth on STO buffered GaAs. It also suggests that the smoothness and crystallinity of BTO film remained satisfactory via a STO interfacial

layer. During the whole growth process, no unidentifiable RHEED patterns were detected, indicates that no interdiffusion and interfacial reaction occur at the interface of the heterostructure.

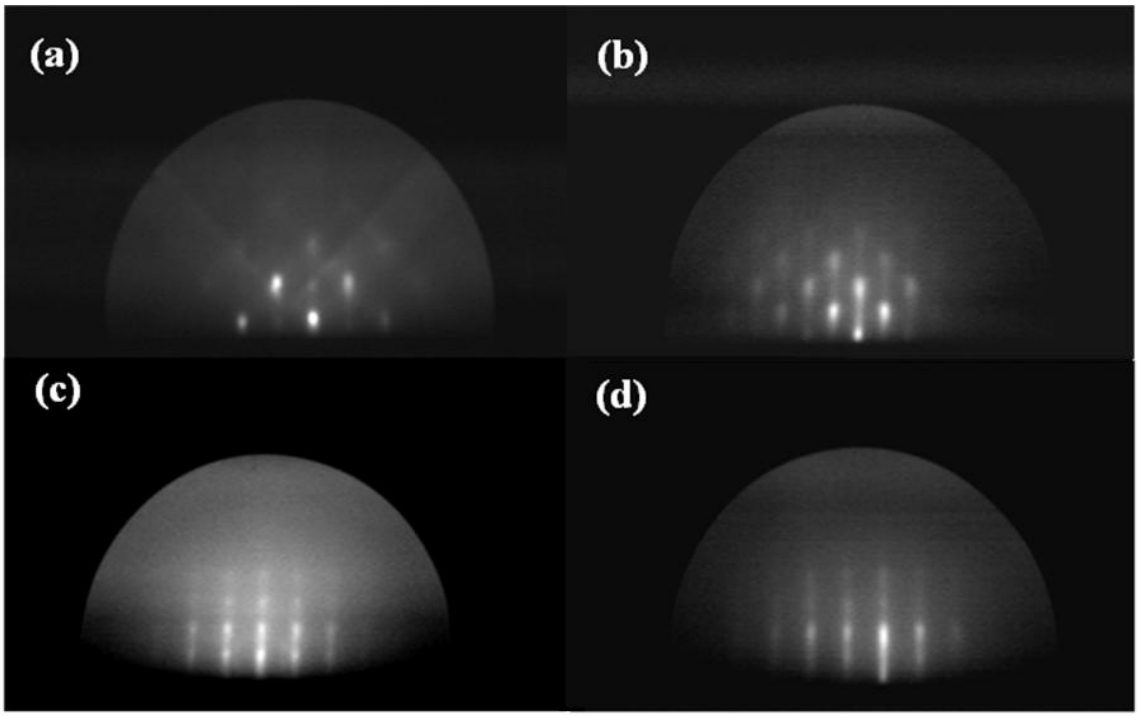

Fig. 4.10 RHEED patterns for heteroepitaxial growth of $BaTiO_3$ thin films on GaAs via $SrTiO_3$ buffer layer with the laser repetition of 1Hz and 2J /cm^2 laser energy density at various thickness: 0 (a), 8 Å $SrTiO_3$ (b),30 Å $SrTiO_3$ (c) and 200 Å $BaTiO_3$

4. 3.3 Crystallization characterized by XRD

Figure 4.11 shows a typical θ-2θ XRD scan of the BTO/STO/GaAs heterostructure. Only the (00*l*) peaks of the BTO appear in the diffraction patterns

indicating that the BTO is basically c-axis oriented growth on STO buffered GaAs substrate. There is no apparent peak corresponding to STO in Fig.2, due to the small thickness of STO layer. To further investigate the degree of in-plane orientations, Φ scan was performed, which reveals that the BTO film is epitaxially grown on the (001) surface of STO and has an in-plane film substrate orientation relationship of [100]BTO//[100]STO//[110]GaAs. The schematic diagram of the BTO/STO/GaAs interface structures is shown in Figure 4.12. The BTO film on STO buffered GaAs has good single crystallinity, which is evident from the small full-width-half-maximum (FWFM) value of the rocking curve of (002) BTO (seen in inset of Fig. 4.11). In addition, the lattice constant *c* of BTO was then calculated to be 4.125 Å, which is slightly larger than that of bulk BTO (*c* =4.01 Å) from powder diffraction. It suggests that the BTO film is slightly compressively strained by the underlying STO buffered layer (*a* =3.903 Å) and the interface of STO buffer layer considerably affects the BTO crystallographic structure.

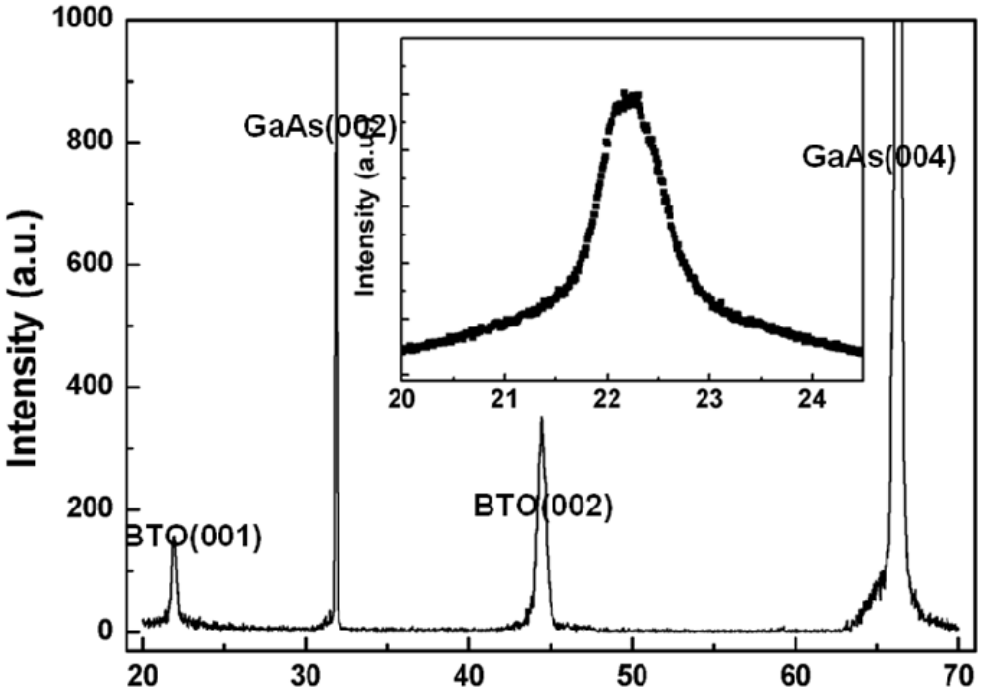

Fig.4.11 XRD pattern of the heteroepitaxial growth $BaTiO_3$ films on GaAs (001), the inset shows the rocking curve of BTO (002).

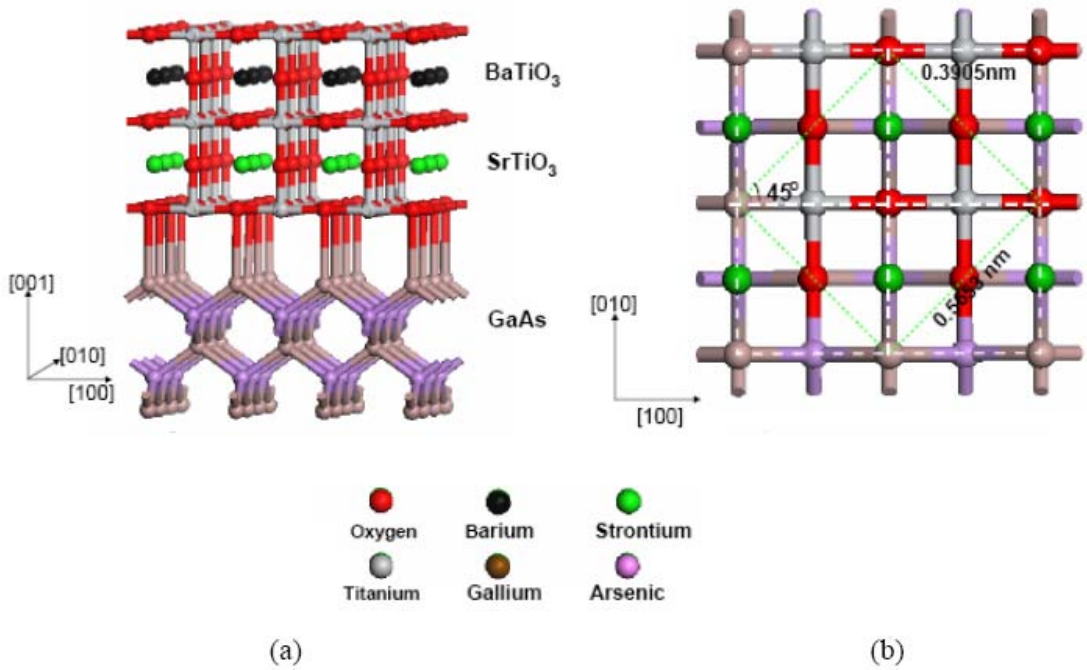

Fig.4.12 Schematic diagram of the BTO/STO/GaAs interface structures. (a) out-of-plane; (b) in-plane

4. 3.4 Interfacial Structure of BTO/STO/GaAs

TEM was employed to investigate the interface of the BTO/STO/GaAs heterostructure. The low-magnification cross-sectional TEM images in Fig. 4.13 reveal a sharp interface structure of the heterostructure. It can be apparently seen that the BTO film with uniform thickness of 150 nm has grown columnarly on a 10-nm-thick STO buffer layer. Selected area diffraction patterns (SAD) taken at A1, A2, A3 are demonstrated in Figure 4.14. The highly ordered electron diffraction spots of BTO lattice also confirmed that the BTO film is highly epitaxially grown on the (001) surface

of STO. The lattice constant *a* of BTO was estimated to be 3.951 Å, which is smaller than that of bulk BTO (a=3.994 Å). This also suggests that the BTO is slightly compressively stressed by the underlying STO layer, which is consistent with the XRD analysis. The high-resolution TEM image in Figure 4.15 reveals an atomical interface character between the BTO and STO buffered GaAs substrate. From the image, a noticeable interfacial layer about 10 nm in thickness can be seen at the interface between the STO buffer and GaAs substrate. This rough interfacial structure could be attributed to the threading dislocations induced by the lattice mismatch during the initial STO growth. This result is consistent with the RHEED analysis. In the general case of cube-on-cube growth using STO buffer, threading dislocations always form at the interface between the film and substrate, and consequently they propagate into whole epilayer along the slip plane, or become nucleation sites for defect formation from the interface [Y. Liang, 2004]. However, in spite of the high density of misfit dislocations in STO buffer layer, the formation of threading dislocations driven to BTO film through the STO buffer is very low. In other words, the interface structure disturbances originated from stracking faults were terminated by inserting STO buffer and hence inducing a good epitaxy of BTO layer.

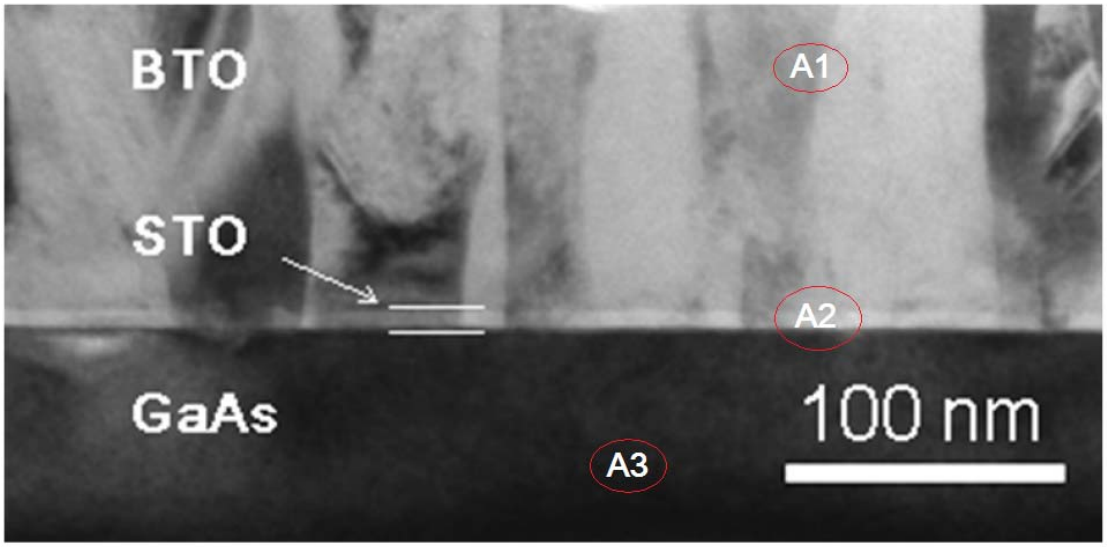

Fig. 4.13 The low magnification cross-sectional transmission electron microscope image of BTO/STO/GaAs.

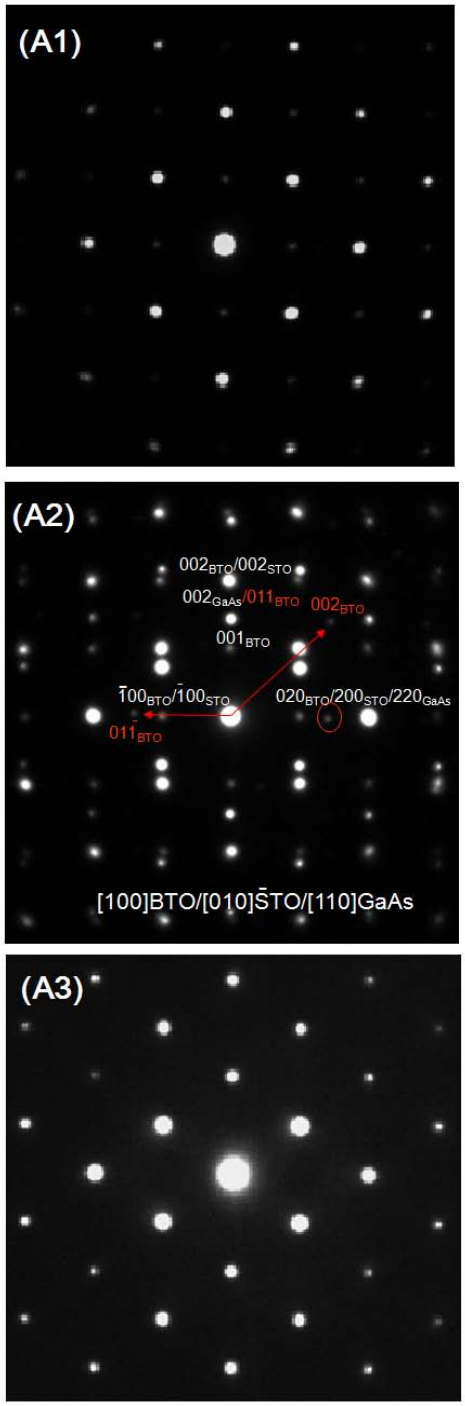

Fig. 4.14 Selected area diffraction patterns of BTO/STO/GaAs taken at A1, A2, A3.

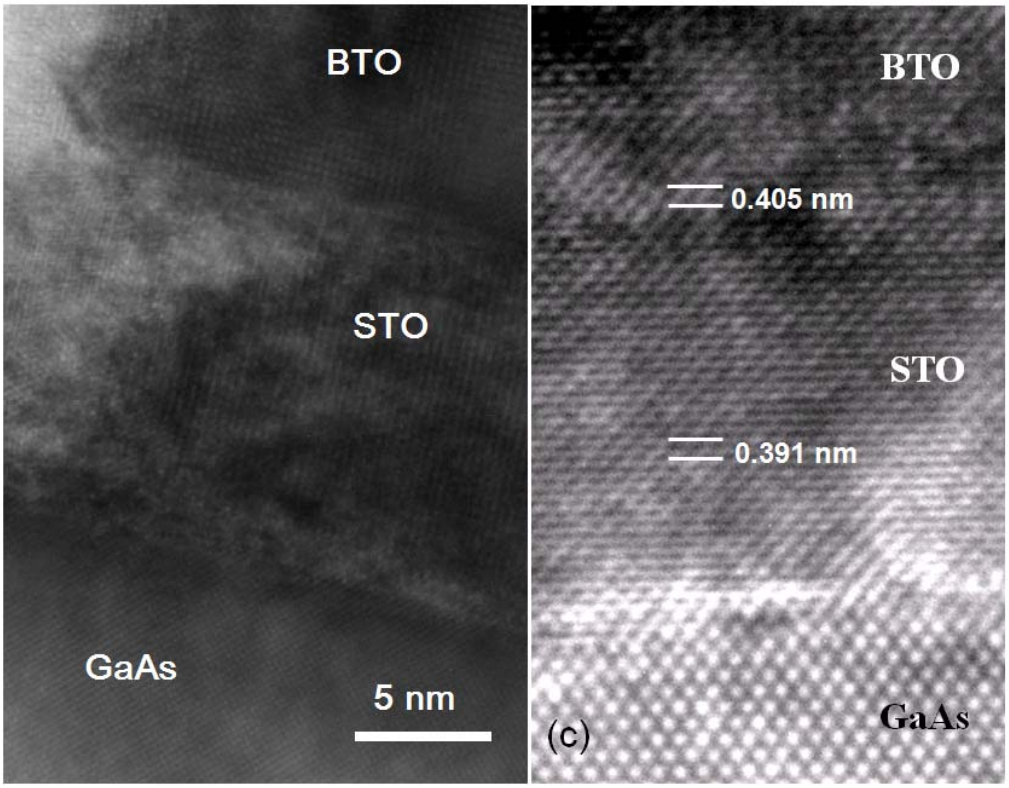

Fig. 4.15 High-resolution TEM image of BTO/STO/GaAs interface. BTO and STO are well crystallized and epitaxially aligned.

4. 3.5 Electrical Characterization of BTO/STO/GaAs

In order to understand the interface effect on electrical properties of the BTO/STO/GaAs heterostructure, the leakage current and polarization properties were measured as a function of electrical field. As shown in Figure 4.16, the leakage current density J of the BTO/STO/GaAs heterostructure is considerably reduced by inserting STO buffer layer under a given electric field. For instance, the value of current density is

2.9×10^{-7} A/cm^2 for BTO thin films deposited on a 10 nm STO buffer layer at a field of 200 kV/cm, almost two orders of magnitude lower than that 1.7×10^{-5} A/cm^2 for BTO thin films without using a STO buffer layer under the same field. Moreover, as seen from Figure 4.17, compared with previous reports on MgO buffered BTO film on GaAs, the BTO/STO/GaAs heterostructure exhibits a typical ferroelectric behavior with a remnant polarization (*Pr*) of 2.5 μC/cm^2 and a electrical coercive field (*Ec*) of 100 kV/cm. Although the measured P-E loop windows are much smaller than the theoretical calculated values, the charge injection was significantly suppressed and the ferroelectric behavior is then enhanced. This is somewhat similar to the improved ferroelectric property in MFIS structures, such as BFO/ZrO/Si [Y.W. Chiang, 2007], $SrBi_2Ta_2O_9$/HfTaO/Si [X.B. Lu, 2008] and many others. These high structure-dependent films always show good performances by inducing a good interfacial layer. Therefore, these well behaved *P-E* loops with a small leakage current in our films can also be considered that the interface between BTO and GaAs is improved by inserting STO as buffer layer, and thus a good epitaxy of BTO layer exhibits an enhanced electrical property.

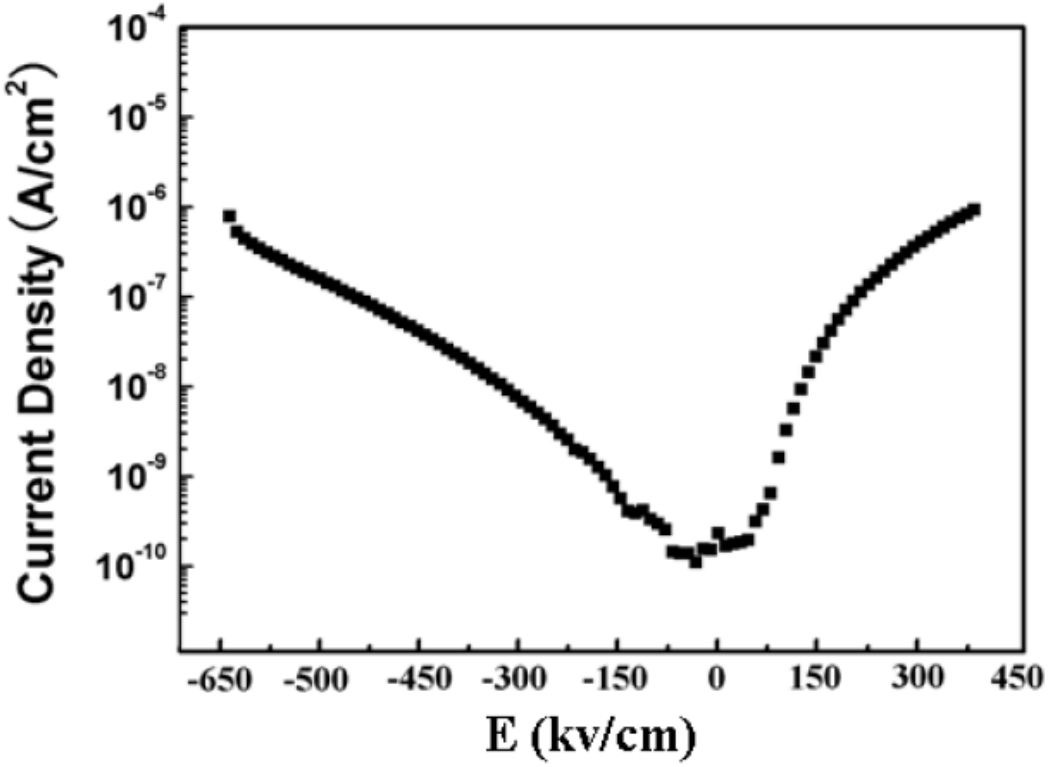

Fig. 4.16 *J-E* property of the BTO/STO/GaAs heterostructure

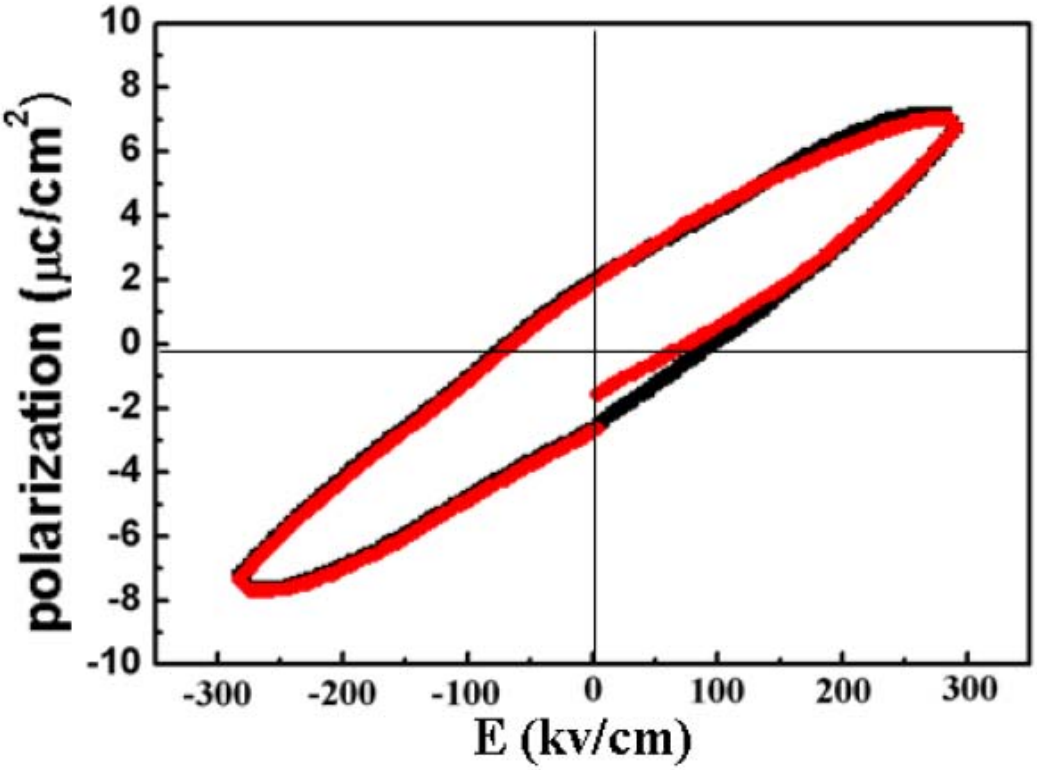

Fig. 4.17 *P-E* loops of the BTO/STO/GaAs heterostructure

4.4 Summary

In this work, epitaxial $SrTiO_3$ thin films have been successfully grown on GaAs substrates by LMBE. The in-plane orientation relationship with substrate is $SrTiO_3$[110]//GaAs[001]. Cross-section TEM confirmed that the STO film is highly epitaxially grown on the (001) surface of GaAs. The surface morphology of films, as observed by AFM, was quite smooth. The dielectric characteristics of STO/GaAs heterojunction were also studied.

Based on STO buffered GaAs substrate, the epitaxial growth of the ferroelectric BTO thin film on GaAs has been achieved. The interface effects on the epitaxial nature and the *P-E* and *J-E* characteristics of the MFIS structure have been systematically investigated. It is found that the interface properties of BTO/GaAs heterostructure are greatly improved by inserting a 10 nm-thick STO buffer layer. The leakage current density of this heterostructure is considerably reduced to 2.9×10^{-7} A/cm^2 at a field of 200 kV/cm. Also the heterostructure exhibit good ferroelectric behavior with a Pr of 2.5μC/ cm^2.

CHAPTER 5

CONCLUSIONS AND SUGGESTIONS FOR FUTURE WORK

5.1 Conclusions

The present research focused on the investigation of the structure and dielectric properties of epitaxial perovskite titanate thin films. The main conclusions can be summarized as follows:

Heterostructures of $SrTiO_3$ (STO)/$YBa_2Cu_3O_y$ (YBCO)/$LaAlO_3$ and STO/YBCO/STO were fabricated by using laser molecular beam epitaxy (L-MBE) technique. The L-MBE technique provides a convenient way of growing oxide thin films under relatively high oxygen pressure, enabling atomic control and characterization of thin film growth process. We have observed different growth modes during the growth of YBCO thin films, depending on the conditions of strain and interface of heterostructures. Atomic force microscope (AFM) was employed to study the surface morphology and the effect of strain on thin film with different thickness. X-ray diffraction (XRD) measurement confirms single orientation (00*l*) of grown YBCO and STO thin films orientation. The Raman spectra of STO films exhibits dramatic difference compared with those of STO single-crystal. Both temperature and frequency

can affect the dielectric properties of STO/YBCO heterostructure in the measurements. The results suggest that strain and defects may contribute to the lowering of symmetry in STO films, and therefore change dielectric properties of STO thin films.

Epitaxial STO thin films have been successfully grown directly on GaAs substrates by L-MBE. The in-plane orientation relationship with substrate is STO[110]//GaAs[001], which means a 45° in-plane rotation of STO with respect to GaAs was occurred. The surface morphology of STO on GaAs was investigated by AFM, showing a smooth surface with a small root-mean square roughness value of 0.84nm. The STO/GaAs interface shows a sharp interface by transmission electron microscopy (TEM). The variation of dielectric properties of STO/GaAs heterostructure was also studied as a function of frequency at room temperature. The dielectric constant of the STO thin film was smaller compared to that of STO bulk, which may be attributed to the effects of bottom electrode GaAs and/or charge dissipation at the oxide/semiconductor interface.

After successfully grown STO thin film directly on GaAs substrates, the epitaxial growth of ferroelectric $BaTiO_3$ (BTO) thin film on 10 nm-thick STO buffered GaAs has been achieved by L-MBE. The interface structure was analyzed by means of reflection high energy electron diffraction and TEM. The perovskite STO buffer layer present a body centered cubic structure by forming an interfacial layer about 10 nm, with the [100]STO//[110]GaAs in-plane relationship. Thereupon, a highly c-oriented BTO was grown on STO/GaAs in a two-dimensional layer by layer mode, leading to a sharp

interface and a significant reduction of mismatch-related defects. The *P-E* and *J-E* characteristics of the BTO/STO/GaAs structure have been systematically investigated. The leakage current density of this heterostructure is 2.9×10^{-7} A/cm^2 at a field of 200 kV/cm. Also the heterostructure exhibit good ferroelectric behavior with a remnant polarization of 2.5μC/ cm^2.

5.2 Suggestions for Future Work

This thesis is devoted to study the structural and dielectric properties of perovskite titanates such as STO. The following are some suggested topics for future research which may be regarded as an extension of the present work.

STO thin films shows great promise for high-frequency microwave applications. Thus, the study of high-frequency property of the heterostructures will be an interesting issue. The dielectric loss of perovskite films plays a critical role in the performance of tunable microwave devices. The relationship between high-frequency dielectric loss and growth mode will be one of further investigation topics.

Although the STO/GaAs and BTO/STO/GaAs heterostructures have been successfully fabricated by L-MBE, a comprehensive understanding of the relationship between structure and electrical properties is still open for investigation. It will be an essential issue to investigate what factors (lattice strain, interface effect, grain size effect, and so on) determine the dielectric and ferroelectric properties of ferroelectric titanates.

STO buffered GaAs substrates make it possible to integrate the perovskite functional materials with semiconductor wafers. Based on the obtained system of STO/GaAs, many functional perovskite thin films such as $Ba_xSr_{1-x}TiO_3$ could be grown subsequently the template. Thus, single-crystal oxide substrates (MgO, $LaAlO_3$, *etc.*) with high cost and small geometries, currently used in tunable microwave devices, could be replaced by commercial semiconductor GaAs compatible with microwave integrated circuits. Moreover, it is promising to incorporate additional magneto-optical and electro-optical functionalities by integrating magnetic and electro-optic oxides with the STO/GaAs heterostructure.

REFERENCES

A. J. Moulson, and Herbert, J. M. *Electroceramics: Materials, Properties, Applications*. Chapman and Hall, New York, USA (1997)

A. K. Pradhan, S. Mohanty, K. Zhang, J. B. Dadson, E. M. Jackson, D. Hunter, R. R. Rakhimov, G. B. Loutts, J. Zhang, and D. J. Sellmyer, *Appl. Phys. Lett.* 86, 012503 (2005)

A. Lin, X. Hong, V. Wood, A. A. Verevkin, C. H. Ahn, R. A. Mckee, F. J. Walker, and E. D. Specht, *Appl. Phys. Lett.* 78, 2034 (2001)

A. Shapere, F. Wilczek (Eds.), *Geometric Phases in Physics*, World Scientific, Singapore (1989)

A. Talin, S. M. Smith, S. Voight, J. Finder, K. Eisenbeiser, D. Penunuri, Z. Yu, P. Fejes, T. Eschirich, J. Curless, D. Convey, and A. Hooper, *Appl. Phys. Lett.* 81, 1062 (2002)

B. M. Kim, T. Brintlinger, E. Cobas, M. S. Fuhrer, H. Zheng, Z. Yu, R. Droopad, J. Ramdani, and K. Eisenbeiser, *Appl. Phys. Lett.* 84, 1946 (2004)

C. Ang, L. E. Cross, Z. Yu, Ruyan Guo, A. S. Bhalla, J. H. Hao, *Appl. Phys. Lett.* 78 2754 (2001)

C. H. Mueller, R. E. Treece, T. V. Rivkin, F. A. Miranda, H. R. Mountinho, A. Swartzlander-Franz, M. Dalberth, and C. T. Rogers, *IEEE Trans. Appl. Supercond.* 7, 3512 (1997).

C. J. Först, C. R. Ashman, K. Schwarz, and P. E. Blöchi, *Nature* 427, 53 (2004)

D. A. Tenne, X. X. Xi, Y. L. Li, L. Q. Chen, A. Soukiassian, M. H. Zhu, A. R. James, J. Lettieri, D. G. Schlom, W. Tian, X. Q. Pan, *Phys. Rev. B.* 69, 174101 (2004)

D. Chen, T. E. Murphy, S. Chakrabarti, J. D. Phillipsa, *Appl. Phys. Lett.* 85, 5206 (2004).

David E. Fulkerson, *IEEE Transactions on Electron Devices* VOL. 39. NO. 3. 745 (1992)

C. L. Jia, K. Urban, S. Hoffmann, R. Waser, *Journal of Materials Research* 13, 2206 (1998).

D. Damjanovic, *Reports on Progress in Physics*, Vol. 61, pp. 1267-1324 (1998).

D. Galt, J. C. Price, J. A. Beall, and R. H. Ono, *Appl. Phys. Lett.* 63, 3078 (1993)

D. L. Polla and L. F. Francis, *Mater. Res. Bull.* 21, 59 (1996)

D. Roy and S. B. Krupanidhi, *Appl. Phys. Lett.* 62, 1056 (1993).

E. Tosatti and R. MartonÆaÂk, *Solid State Commun.*, 92, 167 (1994)

F. A. Miranda, C. H. Mueller, C. D. Cubbage, K. B. Bhasin, R. K. Singh, and S. D. Harkness, *IEEE Trans. Appl. Supercond.* 5, 3191 (1995).

F. Sánchez, M. Varela, X. Queralt, R. Aguiar, and J. L. Morenza, *Appl. Phys. Lett.* 61, 2228 (1992).

F. Sánchez, R. Aguiar, V. Trtik, C. Guerrero, C. Ferrater, and M. Varela, *J. Mater. Res.* 13, 1422 (1998).

G. D. Wilk, R. M. Wallance, J. M. Anthony, *J. Appl. Phys.* 87, 484 (2000)

G. F. Dionne and D. E. Oates, *IEEE trans. Magn.*, 33, 3421 (1997)

G. H. Haertling, *Journal of the American Ceramic Society*, Vol. 82, pp. 797 (1999).

G. Shirane and Y. Yamada, *Phys. Rev.* 177, 858 (1969)

H. Ishiwara, *Integr. Ferroelectr.* 17, 11 (1997)

H. Li, X. Hu, Y. Wei, Z. Yu, X. Zhang, R. Droopad, A. A. Demkov, J. Edwards, Jr., K. Moore, W. Ooms, J. Kulik, and P. Fejes, *J. Appl. Phys.* 93, 4521 (2003).

H. N. AL-Shareef, D. Dimos, M.V. Raymond, R. W. Schwartz and C. H. Mueller, *Journal of Electroceramics*, 1, 145 (1997)

H. Tabata, H, Tanaka, T, Kawai, *Appl. Phys. Lett.* 65, 1970 (1994)

H. Uwe and T. Sakodo, *Phys. Rev. B*, 13, 271 (1976).

H. Vogt, G. Rossbroich, *Phys. Rev. B* 24, 3086 (1981)

I. A. Akimov, A. A. Sirenko, A. M. Clark, J. H. Hao, X. X. Xi, *Phys. Rev. Lett.* 84, 4625 (2000)

J. C. Le Breton, S. Le Gall, G. Jézéquel, B. Lépine, P. Schieffer, and P. Turban, *Appl. Phys. Lett.* 91,172112 (2007).

J. F. Nye, *Physical properties of crystals: their representation by tensors and matrices*, Oxford University Press London (1957).

J.G. Bednorz and K.A. MuÈller, *Phys. Rev. B*, 52, 2289 (1984).

J. H. Chen, C. L. Lia, K. Urban and C. L. Chen, *Appl. Phys. Lett.* 81, 1291 (2002).

J.H. Hao, W. D. Si, X. X. Xi, R. Guo, A. S. Bhalla, and L. E. Cross, *Appl. Phys. Lett.* 76, 3100 (2000)

J. H. Hao, Z. Luo, J. Gao, *J. Appl. Phys*. 100, 114107 (2006)

J. H. Hao, J. Gao, Z. Wang, and D.P. Yu, *Appl. Phys. Lett.*, 87, 131908 (2005)

J. Hemberger, P. Lunkenheimer, R. Viana, R. BoÈhmer, and A. Loidl, *J. Phys.: Condens. Matter*, 8, 4673 (1996).

J. L. Li, J. H. Hao, Y.R. Li , *Appl. Phys. Lett.* 91, 131902 (2007).

J.M. Worlock and P.A. Fleury, *Phys. Rev. Lett.*, 19, 1176 (1967).

J. Q. He, S. Regnery, C. L. Jia, Y. L. Qin, F. Fitsilis, P. Ehrhart, R. Waser, K. Urban, and R. H. Wang, *J. Appl. Phys.* 92, 7200 (2002)

J. S. Wu, C. L. Jia, K. Urban, J. H. Hao, X. X. Xi, *J. Mater. Res.* 16 3443 (2001).

J. Wang, H. Zheng, Z. Ma, S. Prasertchoung, M. Wuttig, R. Droopad, J. Yu, K. Eisenbeiser, and R. Ramesh, *Appl. Phys. Lett.* 85, 2574 (2005)

L. Eyraud (Ed.), *Dielectriques Solides Anisoptropes et Ferroelectricite* Gauthier-Villars, Paris (1967)

K.A. Müller and H. Burkard, *Phys. Rev. B*, 19, 3593 (1979)

K.A. Müller, W. Berlinger, and E. Tosatti, *Z. Phys. B*, 92, 277 (1991)

K. Abe, S. Komatsu, *Japanese Journal of Applied Physics Part 1-Regular Papers Short Notes & Review Papers.* 31, 2985 (1992)

K. D. Choquette, K. M. Geib, C. I. H. Ashby, R. D. Twesten, O. Blum, H.Q. Hou, D. M. Follstaedt, B. E. Hammons, D. Mathes, R. Hull, *IEEE J. Sel. Top. Quantum Electron.* 3, 916 (1997).

L. Ryen, Olsson E, Madsen LD, X. Wang, C. N. L. Edvardsson, S. N. Jacobsen, U. Helmersson, S. Rudner, *J. Appl. Lett.* 83, 4884 (1998)

M. A. Saifi and L. E. Cross, *Phys. Rev. B.* 123, 2 (1970)

M. E. Lines and A. M. Glass, *Ferroelectrics and related materials*, Oxford, (1977).

M. Hawley, I. D. Raistrick, J. G. Beery, and R. J. Houlton, *Science* 251 1587 (1991).

M. Hong, J. Kwo, A. R. Kortan, J. P. Mannaerts, and A. M. Sergent, *Science* 283, 1897 (1999)

M. Hong, Z. H. Lu, J. Kwo, AR. Kortan, J. P. Mannaerts, J. J. Krajewski, *Appl. Phys. Lett.* 76, 312 (2000).

M. Ishida, S. Tsuji, K. Kimura, H. Matsunami, and T. Tanaka, *J. Cryst. Growth* 45, 393 (1978).

M. Lippmaa, N. Nakagawa, M. Kawasaki, *Appl. Phys. Lett.* 74, 3543 (1999)

M. Passlack, J. Abrokwah, R. Droopad, Z. Yu, C. Overgaard, S. Yi, M. Hale, J. Sexton, A. Kummel, *IEEE Electron Device Lett.* 23, 508 (2002).

M. Yoshimoto, H. Ohkubo, N. Kanda, H. Koinuma, K. Horiguchi, M. Kumagai, K. Hirai, *Appl. Phys. Lett.* 61, 2659, (1992)

N. Sai, B. Meyer, and D. Vanderbilt, *Phys. Rev. Lett.* 84, 5636 (2000).

N. W. Schubring, J. V. Mantese, A. L. Micheli, A. B. Catalan, and R. Z. Lopez, *Phys. Rev. Lett.* 68, 1778 (1992).

O. Auciello, J. F. Scott, and R. Ramesh, *Phys. Today* 51, 22 (1998)

O. Nakagawara, M. Kobayashi, Y. Yoshino, Y. Katayama, H. Tabata, and T. Kawai, *J. Appl. Phys.* 78, 7226 (1995)

P. Ghosez, *Microscopic properties of ferroelectric oxides from first principles: Selected topics* Troisieme Cycle de la Physique en Suisse Romande, Lausanne (2002)

R. A. Cowley, *Phys. Rev. Lett*, 9, 159 (1962)

R. Auer, E. Brecht, K. Herrmann, and R. Schneider, *Physica C* 299, 177 (1998)

R. A. Mckee, F. J. Walker, M. F. Chisholm, *Phys. Rev. Lett.* 81, 3014 (1998).

R. A. McKee, F. J. Walker, M. F. Chisholm, *Science* 293, 461 (2001)

R. A. McKee, F. J. Walker, M. B. Nardelli, W. A. Shelton, and G. M. Stocks, *Science* 300, 1726 (2003)

R. Chau, *et al. IEEE Trans. Nanotechnol.* 4, 153 (2005).

R. E. Cohen, and H. Krakauer, *Phys. Rev. B* 42, 6416 (1990).

R. E. Cohen, *Nature* 358, 136 (1992).

R. E. Williams, *Gallium Arsenide Processing Techniques* Artech House, Dedham, MA, (1984)

R. Ramesh, A. Inam, W. K. Chan, B. Wilkens, K. Myers, K. Remschnig, D. L. Hart, and J. M. Tarascon, *Science* 252, 944 (1991)

R. Ramesh, W. K. Chan, B. Wilkens, Gilchrist H, Sands T, J. M. Tarascon, Keramidas V G, Fork D K, Lee J and Safari A, *Appl. Phys. Lett.* 61 1537 (1992)

R. Resta, *J. Phys. Condens. Matter* 12, R107 (2000).

R. Viana, P. Lunkenheimer, J. Hemberger, R. BoÈhmer, and A. Loidl, *Phys. Rev. B*, 50, 601 (1994).

R. W. Babbit, T. E. Koscica, and W. C. Drach, *Microw. J.* 35, 63 (1992)

S. Gupta, R. S. Katiyan, *J. Raman. Spectrosc.* 32, 885 (2001)

S. Migita and S. Sakai, *J. Appl. Phys.* 89, 5421(2001)

S. Y. Yang, Q. Zhan, P. L. Yang, M. P. Cruz, Y. H. Chu, R. Ramesh, Y. R. Wu, J. Singh, W. Tian, and D. G. Schlom, *Appl. Phys. Lett.* 91, 022909 (2007)

T. E. Murphy, D. Chen, J. D. Phillips, *Appl. Phys. Lett.* 85, 3208 (2004).

T. Tambo, T. Nakamura, K. Maeda, H. Ueba, C. Tatsuyama, *Japanese Journal of Applied Physics Part 1-Regular Papers Short Notes & Review Papers* 37, 4454, (1998)

T. Van Duzer, *IEEE Trans. Appl. Supercond.* 7, 98 (1997)

T. Yamada, N. Wakiya, K. Shinozaki, and N. Mizutani, *Appl. Phys. Lett.* 83, 4815 (2003).

V. K. Varadan, D. K. Ghodgaonkar, V. V. Varadan, J. F. Kelly, and P. Glikerdas, *Microw. J.* 35, 116 (1992)

V. N. Denisov, B. N. Mavrin, V. B. Podobedov, *Phys. Rep.* 151, 1 (1987)

V. Nagarajan, S. P. Alpay, C. S. Ganpule, *et. al*, *Appl. Phys. Lett.* 77, 438 (2000).

V. Vonk, S. J. van Reeuwijk, J. M. Dekkers, S, Harkema, A.J.H.M. Rijnders, H. Graafsma, *Thin Solid Films* 449, 133 (2004)

W. Chang, S. W. Kirchoefer, J. A. Bellotti, S. B. Qadri, and J. M. Pond, *J. Appl. Phys.* 98, 024107 (2005)

Woo Young Park, Kun Ho Ahn and Cheol Seong Hwang, *Appl. Phys. Lett.* 83, 4387 (2003).

X.B. Lu, K. Maruyama, H. Ishiwara, *J. Appl. Phys.* 103, 044105 (2008).

X. H. Zhu, W. Peng, J. Li, Y. F. Chen, H. Y. Tian, X. P. Xu, D. N. Zheng, *J. Appl. Phys.* 97, 014108 (2005)

X. X. Xi, Hong-Cheng Li, Weidong Si, A. A. Sirenko, I. A. Akimov, J. R. Fox, A. M. Clark and J. H. Hao, *Journal of Electroceramics* 4, 393, (2000)

Xu, Y. *Ferroelectric Materials and Their Applications*. North-Holland, New York, USA (1991).

Y. Liang, J. Kulik, T. C. Eschrich, R. Droopad, Z. Yu, P. Maniar, *Appl. Phys. Lett.* 85, 1217 (2004).

Y. Wang, C. Ganpule, B. T. Liu, H. Li, K. Mori, B. Hill, M. Wuttig, R. Ramesh, J. Finder, Z. Yu, R. Droopad, and K. Eisenbeiser, *Appl. Phys. Lett.* 80, 97 (2005).

Y.W. Chiang, J.M. Wu, *Appl. Phys. Lett.* 91, 142103 (2007)

Y. Mukunoki, N. Nakagawa, T. Susaki, H.Y. Hwang, *Appl. Phys. Lett.* 86, 171908 (2005)

Y. Z. Yoo, P. Ahmet, Z. W. Jin, K. Nakajima, T. Chikyow, M. Kawasaki, Y. Konishi, Y. Yonezawa, J. H. Song, and H. Koinuma, *Appl. Phys. Lett.* 82, 4125 (2003).

Z. P. Wu, W. Huang, K. H. Wong, J. H. Hao, *J. Appl. Phys.* 104, 054103 (2008).

Z. Wamg, V. Kugler, U. Helmersson, N. Konofaos, E. K. Evangelou, S. Nakao, and P. Jin, *Appl. Phys. Lett.* 79, 1513 (2001)